



UNIVERSITÀ DEGLI STUDI DI PARMA
DIPARTIMENTO DI FISICA E SCIENZE DELLA TERRA

Corso di Laurea Magistrale in
FISICA

**Controlling dynamics in flatland through
curvature-composition coupling in membranes.**

**Controllo della dinamica in sistemi quasi-2D
tramite accoppiamento curvatura-composizione
nelle membrane.**

Relatore:
Luigi Cristofolini

Correlatore:
Pietro Cicutà

Candidato:
Luigi Feriani

ANNO ACCADEMICO 2012/2013

Contents

1	Introduction	6
2	Background	8
2.1	Lipid membranes: model systems for biological processes	9
2.2	Liquid-liquid phase separation	11
2.2.1	Role of cholesterol	14
2.3	Bending energy	16
2.4	Inducing curvature on ternary membranes	18
2.5	Simple estimates of membrane bending on topographically patterned surfaces	19
3	Materials and experimental methods	21
3.1	Soft Lithography	21
3.1.1	Poly(dimethylsiloxane) chemistry	21
3.1.2	Surface preparation protocol	22
3.1.3	Surface characterisation	26
3.2	Giant Unilamellar Vesicles	28
3.2.1	Ternary lipid mixture	28
3.2.2	Electroformation protocol	30
3.2.3	Sample chamber	32
3.2.4	Epifluorescence microscopy	33
4	Analysis and results	34
4.1	Tracking	34
4.1.1	Features location	38
4.2	Mean Square Displacement analysis	38
4.2.1	Mean Square Displacement calculation	38
4.2.2	Indirect assessment of the contact area	42

<i>CONTENTS</i>	3
4.2.3 Dependence on the radius	45
4.3 Caging analysis	48
4.4 Discussion	53
5 Concluding remarks and future work	54
Bibliography	55

List of Figures

2.1	Structure of phosphatidylcholine	9
2.2	Liquid phases	11
2.3	Miscibility phase diagrams of four ternary mixtures show common features.	12
2.4	Detailed phase diagram of a system close to the one studied in this thesis	15
2.5	Equilibrium shapes and phase morphologies of phase-separated vesicles	18
2.6	3D model of the deformation induced by the PDMS features on the membrane	20
3.1	PDMS chemical structure	22
3.2	PDMS master preparation	23
3.3	PDMS double-casting	25
3.4	AFM: tip-sample convolution	26
3.5	AFM and SEM images of the PDMS surface	27
3.6	Chemical structures of the lipids used in this work, and phase diagram from the literature	29
3.7	Diagram of the electroformation chamber	31
3.8	Diagram of the imaging chamber	32
4.1	Filtering and feature-recognition	35
4.2	Tracking of L_d domains, showing pinning on the bumps	36
4.3	PDMS features (“bumps”) location	37
4.4	Tracking of L_d domains highlighting interaction with features	39
4.5	Distribution of the Mean Square Displacement and of the diffusion coefficient, showing the different behaviour for L_d domains on bumps and not on bumps.	40

4.6	Example of MSD curve	41
4.7	Distance from the centre of the GUV	43
4.8	Effect of the distance from the centre of the GUV	44
4.9	Scatter plot of the Mean Square Displacement	46
4.10	Scatter plot of the diffusion coefficient, highlighting the reduced mobility of L_d domains on bumps	47
4.11	Trapping despite the drift of the GUV	48
4.12	Effects of caging: the MSD/4D curve deviates from the line describing the Brownian motion	50
4.13	Caging dependence on the radius, in qualitative agreement with confined Brownian motion simulations	52
4.14	“Depinning” due to domain-domain interaction	53

Chapter 1

Introduction

Over the last decades, artificial lipid bilayers have become an increasingly popular topic for research, as they are an interesting system from many different perspectives.

Aside from their self-assembling nature, that makes them relatively easy to manipulate in ambient conditions, they are a useful 2D model system to study new physics questions. In biology, their importance can not be overestimate, as they can approximate various aspects of biological membranes, which in turn are a fundamental component of the cell. In particular, multicomponent lipid membranes are the simplest model to study liquid-liquid phase separation, possibly the basis to the lipid “rafts” formation in cell plasma membranes.

My work focuses on the influence of curvature on the lateral organisation of liquid-liquid phase separated lipid bilayers. This particular aspect is very interesting for biology, as it could shed some light on the sensitivity to the curvature shown by some membrane protein, or on the growth of actin filaments, that seems to be influenced by curvature. Moreover, understanding how phase separated bilayers laterally organise in presence of locally induced curvature may lead to an active manipulation of such mechanism, leading to technological applications.

To force the lipid membranes to locally assume a certain curvature a microstructured poly(dimethylsiloxane) surface was employed.

Therefore in this report after a brief literature review and background information ([chapter 2](#)) I will present the experimental methods employed, which cover the crafting of the microstructured surface, the preparation of lipid bilayers, and the imaging methods ([chapter 3](#)). The analysis performed

will be reported in [chapter 4](#), while [chapter 5](#) will provide an overview of the results obtained, alongside with promising aspects that could be the basis for future research.

Chapter 2

Background

Lipids are a group of naturally occurring molecules, including, fats, waxes, sterols, and phospholipids. Instead of being defined by molecular structure (that can significantly vary in this group) the category is generally considered to include small molecules with amphiphilic or hydrophobic behaviour [85]. Most lipids are composed of acyl chains linked to an ester group (e.g. phospholipids and fats). Many lipids are surfactants, therefore when in an aqueous environment they self-assemble in a variety of structures. Depending on a number of factors as concentration, molecular geometry, and temperature, lipids can form different aggregates such as micelles, bilayers, bulk phases (lamellar, hexagonal, etc.) as well as bicontinuous configurations [20, 14]. The aggregation process is usually driven by many factors, as steric effects, hydrophobic effects and curvature modulus.

This work is focused on lipid mixtures containing mostly phospholipids, in particular phosphatidylcholines (PC), as they are a major component of biological membranes. Phospholipids are composed of a hydrophilic head, that includes a phosphate group and a glycerol, and two hydrophobic tails, typically hydrocarbon chains [85]. Phosphatidylcholines are distinguished from other phospholipids by the presence of a choline molecule in the hydrophilic head [85] (see Figure 2.1).

The shape of lipid molecules is generally cylindrical, leading them to assemble in locally flat bilayers [35]. The shape of the single molecule is determined by the space occupied by its average motion, which is heavily dependent on the length and saturation of its acyl chains. A double bond between two carbon atoms yields a bend in the hydrocarbon chain, therefore increasing the effective volume occupied and hindering close packing with

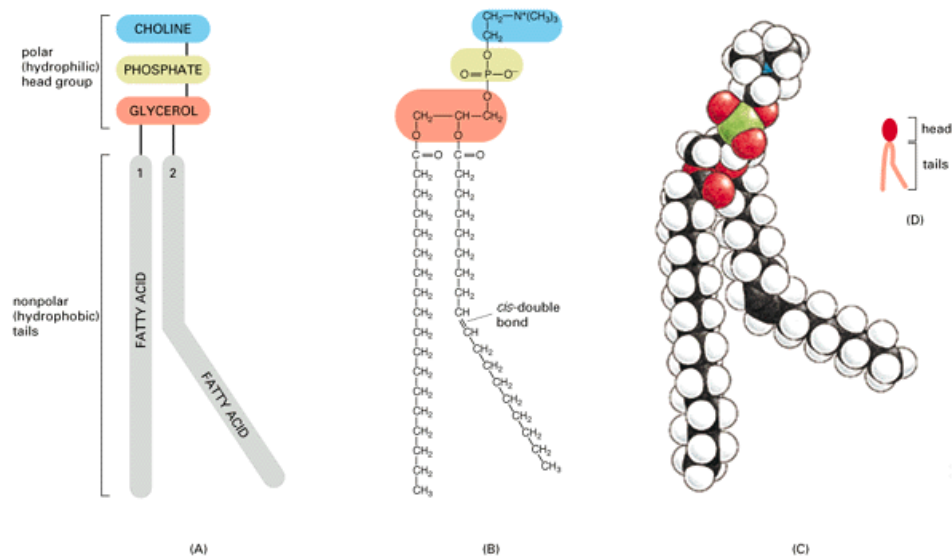


Figure 2.1 – Structure of phosphatidylcholine. Schematic representation of a phosphatidylcholine, that highlights the two main parts of a phospholipid: the hydrophilic head group and the hydrophobic tails). Taken from [1].

neighbouring molecules.

The average surface area per molecule is generally between 65 and 70\AA^2 in a typical phospholipid bilayer. This quantity is basically not influenced by the hydrocarbon chain length [46], that has instead been found to have a linear relationship with the bilayer thickness (typically $3 - 4\text{nm}$) [46].

2.1 Lipid membranes: model systems for biological processes

The study of the coupling between composition and curvature in lipid membranes is relevant in many different fields.

First of all, lipid membranes are in general a nice example of quasi 2D systems, therefore they represent a good model system to investigate ordering in two dimensions. In particular, an improved comprehension of the mechanism of sorting in laterally organised ternary membranes may possibly lead to their manipulation to follow a pattern on the nano- or micro-scale. A patterned, phase separated membrane may then be employed in nano- or micro-structured sensors [9], for example in combination with the phenomenon of plasmonic resonance.

Moreover, the ability of forcing a lipid membrane to assume a desired curvature can be useful to study the curvature sensitivity of membrane protein [59, 55], or the influence of curvature on the growth of actin filaments [24]. The main reason the behaviour of lipid bilayers is being studied, though, is again related to their biological relevance.

Over the last 30 years evidence has emerged of lateral heterogeneity and organisation among lipids in biological membranes [41, 49, 64], going against the “fluid mosaic model”. This model, which was dominant for biological membranes, pictures the membrane as a passive “lipid sea”, in which the proteins motion is purely diffusive [19].

The new model proposed after the new observation is the “raft model” [72], that expects the biological membrane to be laterally organised because of the assembly of certain lipid species into domains, called “lipid rafts”. In this model, lipid raft are introduced as functional microdomains that could selectively include or exclude proteins, therefore having a key role in the membrane transport and in intracellular signalling [72]. Subsequent studies have then linked these rafts with other different processes in the life of a cell, such as adhesion, endocytosis, protein organisation, apoptosis, and lipid regulation [72, 18, 81].

The interest for multicomponent lipid bilayers showing lateral organisation has consequently grown (as the number of papers on the topic clearly states), hoping that understanding phase separation in model multicomponent lipid membranes could help explaining the formation of such structures [17, 69].

Even if biological membranes are composed of thousands of lipid species and have high protein concentration, they seem to exhibit a similar thermodynamical behaviour to a ternary system made of a saturated lipid, an unsaturated one and a sterol [81, 69]. The typical behaviour, common to a wide range of proportions of the components of ternary mixtures, is a phase coexistence of regions enriched in the saturated lipid and cholesterol, and regions enriched in the unsaturated lipid [81, 79] (see Figure 2.2). These regions are formed in the first place because of the net interaction between lipids (sum of various contributions as van der Waals forces, electrostatic and hydrophobic forces) resulting in a preference for demixing between saturated and unsaturated lipids. The entropic contributions leads to the usual behaviour of a phase separation below a critical temperature (T_c , which is strongly

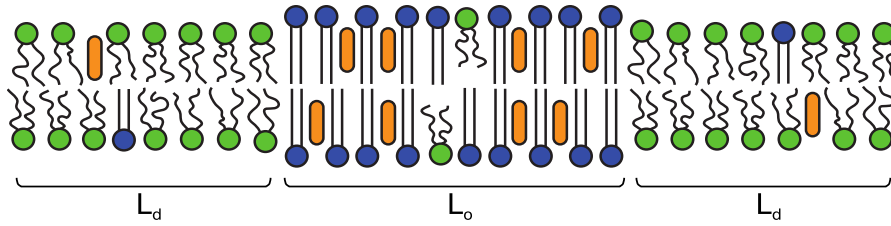


Figure 2.2 – Liquid phases differ in composition, order and thickness. Schematic representation of a ternary lipid bilayer showing the two different liquid phases. The L_o phase, where the lipid with high melting temperature (blue) and the sterol (orange) are predominant, and the L_d phase, mainly populated by the low melting temperature lipid (green). The picture also shows the difference in thickness between the two phases. From [23].

dependent on the lipid species and their proportions), and a single mixed phase above it [68]. Since these ternary saturated/unsaturated/cholesterol model systems have shown to be a basic yet representative approximation for the behaviour of biological membranes, many studies have focused on understanding the phenomenon of phase separation they present, hoping to get some insight into a general mechanism of lateral organisation in biological membranes.

2.2 Liquid-liquid phase separation

A wide variety of ternary lipid mixtures containing a high melting temperature (T_m) lipid (usually with saturated acyl tails), a low T_m one (usually unsaturated) and a sterol have been shown to exhibit coexistence of liquid phases [83], named liquid-disordered (L_d) and liquid-ordered (L_o). These liquid phases have been observed both in Giant Unilamellar Vesicles (GUVs) and in supported bilayers.

Both phases are characterised by fast lateral diffusion, high rotational freedom and short range order, but they present some important differences in both composition and physical properties [28]. The L_o phase is enriched in the saturated lipid, this causing a more effective packing of the lipid molecules (hence the name “liquid-ordered”) than in the L_d phase, where the unsaturated lipid, the dye and other impurities partition. The close packing of lipids with saturated tails also causes the L_o membrane to be thicker.

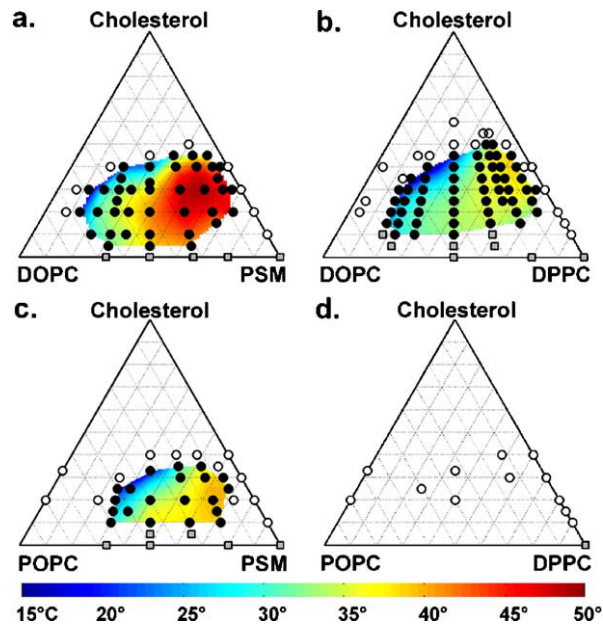


Figure 2.3 – Miscibility phase diagrams of four ternary mixtures show common features. Miscibility phase diagrams reported for (a) PSM/DOPC/Cholesterol, (b) DPPC/DOPC/Cholesterol, (c) PSM/POPC/Cholesterol, (d) DPPC/POPC/Cholesterol. Black circles indicate compositions that showed coexisting liquid phases, open circles compositions that only showed a single mixed phase for temperature as low as 10 °C while grey squares correspond to compositions with only gel/liquid phase coexistence. The coloured area reports the extrapolated fit of measured mixing temperatures T_c . Comparing these phase diagrams reveals an interesting similarity in the shape of the boundaries of the liquid-liquid coexistence region across different mixtures. The diagrams also show the behaviour of the binary mixture obtained by omitting cholesterol: as explained in section 2.2.1 they only present a gel/liquid coexistence. Figure taken from [83].

The difference in thickness has been characterised with AFM measurements [7, 44], and found to be in the order of 1 nm, but dependent on the point of the diagram phase (the thickness difference diminishes as the critical point is approached) [13].

Lipid domains behaviour is determined mainly by two physical quantities: the line tension σ (2D analogue of surface tension) and the membrane viscosity μ . The former, minimising the energy cost of the phase boundaries, is responsible for the roundish shape of lipid domains. It has been characterised by flicker spectroscopy of fluorescently labelled domains in ternary GUVs [30], and by AFM on supported lipid bilayers [13]. Membrane viscosity controls instead the scale of diffusion of domains and inclusions, and has been estimated from the diffusion of lipid domains [10, 62].

It is important to note that the lipid domains have been shown to be in registry between the two leaflet of the bilayer, due to interaction between tails [39, 12, 11]. This means that there is matching between the positions of the domains on the two layers: simulations state that mismatch between the two leaflet is minimal, in the order of tens of lipids in a domain [52].

The bilayer phase behaviour depends strongly on composition and temperature, but it has been shown that also pressure influences the membrane structure [6, 57, 86]. Phase diagrams have been constructed for many lipid mixtures using several different techniques, such as fluorescence microscopy on GUVs [83], fluorescence spectroscopy [16], NMR [84, 15], and X-ray and neutron scattering studies (see [38, 26] and references therein), although so far the exact shape of phase boundaries has not been found. As shown in Figure 2.4 different techniques are still not in complete agreement, especially on size of the coexistence regions and slope of the phase boundaries.

The critical behaviour of ternary model lipid membranes has been studied in recent works by looking at the fluctuations of the shape of the domains with fluorescence microscopy and by AFM (in GUVs and supported bilayers respectively) [13, 30]. The scaling of the line tension (obtained by an analysis of thermal fluctuations of the domains) and of the correlation length close to the critical temperature has been found to be described by a critical exponent, identifying this system as belonging to the Ising 2D class of universality [74].

2.2.1 Role of cholesterol

Cholesterol (or any other sterol) plays a fundamental role in the phase behaviour of ternary membranes. It is concentrated mostly in the L_o phase, in the hydrophobic environment provided by the tails, thus hindering the close packing of the phospholipids. This causes the phospholipid+cholesterol bilayer to show a fluid-like behaviour even at temperatures lower than the melting temperature of the phospholipid alone.

Thanks to the shape of its molecule and its hydrophobicity, cholesterol can move easily between leaflets of the bilayer, and it is likely to enhance the registering of domains [40, 43].

Lack of cholesterol in a ternary lipid mixture has been shown to cause the remaining binary mixture (saturated/unsaturated lipid) not to show the $L_d - L_o$ coexistence. Instead every phase transition would involve a gel phase (see Figures 2.3 and 2.4). In binary lipid mixtures the mixing temperature would fall between the melting temperatures of the two lipids [83].

Cholesterol presence affects many properties of lipid bilayers: the increasing of the cholesterol fraction yields an increasing of the bilayer's thickness [56] and rigidity, changing the elasticity of the membrane [50]. This can have an effect on the sorting mechanism of membrane protein and on their functions, since they are strongly influenced by these parameters [2]. The large gradient in cholesterol concentration across the cellular secretory system may imply that this mechanism is actively exploited by the cell [72, 21, 54].

2.3 Bending energy

The shape of a lipid vesicle can be calculated by minimising the total energy functional under the constraints of fixed area and volume. Given a certain area per molecule, at constant temperature and constant number of molecules the bilayer area can be considered fixed. The volume is instead controlled by the difference in osmolarity between the inner and outer solution: since the membrane has some permeability to water [27], a large difference in osmolarity would cause a net water flow through the membrane until the osmotic equilibrium is reached or the GUV bursts [5].

The free energy for a liquid-liquid phase-separated lipid vesicle has various contributions, arising from bending resistance, lateral tension and line tension of the phase boundaries [4]. The interplay between these contributions causes the phase-separated vesicles to show a wide variety of behaviours and shapes under different conditions, as extensively reported in [4].

Following [36], for a vesicle that presents two liquid phases α and β the total energy can be written as

$$F = F_m + F_b + F_G, \quad (2.3.1)$$

where F_m and F_G are, respectively, the normal and Gaussian bending energy, while

$$F_m = A^{(\alpha)} f^{(\alpha)} + A^{(\beta)} f^{(\beta)} + F_l \quad (2.3.2)$$

denotes the free energy of the mixture ($A^{(\alpha)}$ and $A^{(\beta)}$ are the total areas of the two phases, $f^{(\alpha)}$ and $f^{(\beta)}$ their free energy densities). F_l is the energy of the phase boundaries, defined as

$$F_l = \sigma \int_{\partial\alpha} dl \quad (2.3.3)$$

where $\partial\alpha$ is the phase boundary.

Supposing to have N domains of the phase α in a continuous phase β , the bending energies F_b and F_G can be written as

$$F_b = \frac{\kappa^{(\alpha)}}{2} \sum_{i=1}^N \int_{\alpha_i} dA \left(C_1 + C_2 - C_0^{(\alpha)} \right)^2 + \frac{\kappa^{(\beta)}}{2} \int_{\beta} dA \left(C_1 + C_2 - C_0^{(\beta)} \right)^2 \quad (2.3.4)$$

and

$$F_G = \kappa_G^{(\alpha)} \sum_{i=1}^N \int_{\alpha_i} dA C_1 C_2 + \kappa_G^{(\beta)} \int_{\beta} dA C_1 C_2. \quad (2.3.5)$$

Here $\frac{1}{2}(C_1 + C_2)$ and $C_1 C_2$ are local quantities, and denote respectively the mean and gaussian curvature of the lipid bilayer [36]. The bending moduli ($\kappa^{(\alpha)}$, $\kappa^{(\beta)}$, $\kappa_G^{(\alpha)}$, and $\kappa_G^{(\beta)}$) and the spontaneous curvatures (C_0^α and C_0^β) are constants, since the membrane is taken to be homogeneous within each domain [36].

Equations (2.3.1)-(2.3.5) don't take into account the coupling between monolayers, which would be important if the flip-flop between the two monolayer was strongly suppressed. However, for phospholipid-cholesterol mixtures, this coupling should not be relevant, because of the high flip-flop rate of cholesterol molecules [36].

It is possible to link the bending modulus with the stretching modulus of the bilayer by considering the stretching and compression of the two leaflets, with respect to the neutral surface of the membrane (i.e. the bilayer midplane) [5]. By doing so, one can find that the bending modulus κ of a bilayer is proportional to the stretching modulus K and to the square of the bilayer thickness h [73]: $\kappa \propto K h^2$. Both the measurements [77, 89] and the calculations [37, 29] of the bending modulus of lipid membranes are in agreement with this. In addition, again from [77, 89, 37, 29] it emerges that in liquid-liquid phase-separated lipid membranes the L_o phase has a greater bending modulus than the L_d phase.

While for a uniform GUV the geometric figure that yields minimal energy is spherical, when two phases with different bending modules coexist the energy functional can be minimised by other configurations [70], therefore allowing the GUV to take spectacular shapes as those observed in [4] and reported in Figure 2.5.

A useful parameter in the description of the shape of Giant Unilamellar Vesicle is the volume-to-area ratio, defined as

$$v \equiv \mathcal{V}/\mathcal{V}_{sp}, \quad \text{where } \mathcal{V}_{sp} \equiv \frac{4\pi}{3} \left(\frac{\mathcal{A}}{4\pi} \right)^{\frac{3}{2}} \quad (2.3.6)$$

is the volume of a sphere with the same area \mathcal{A} of the vesicle. This geometric quantity ranges from 0 (a completely deflated vesicle) to 1 (perfectly spherical), and represents a control parameter that can be varied by changes in temperature and osmotic conditions. Since thermal expansivity is larger

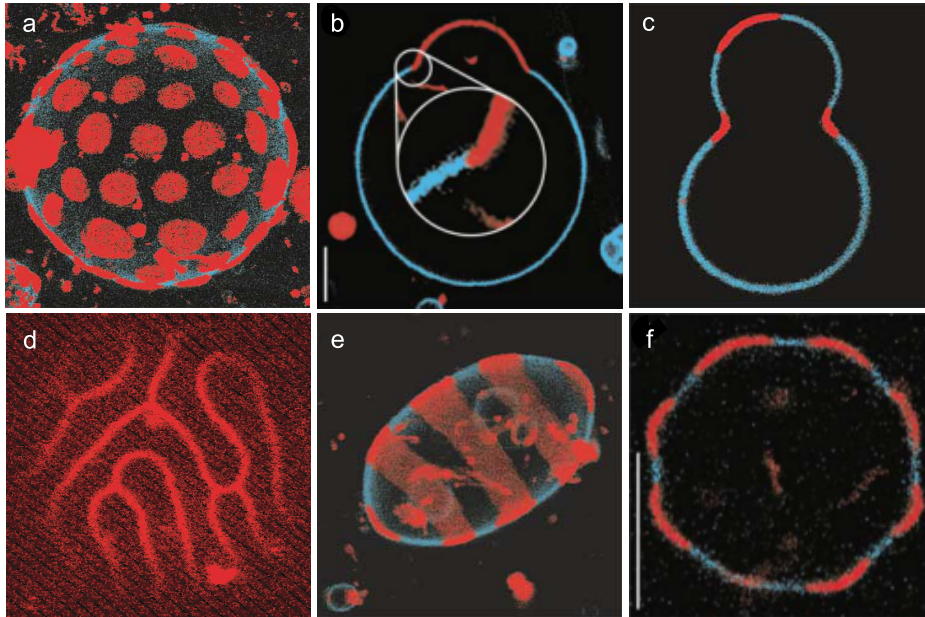


Figure 2.5 – Equilibrium shapes and phase morphologies of phase-separated vesicles. Two-photon microscopy images of ternary vesicles showing liquid-liquid phase-separation. L_d phases are shown in red, L_o in blue. **(a)** Continuous L_o phase, L_d domains budding out of the vesicle. **(b)** Detail of the separation between the two phases. **(d)** Labyrinthine L_d domains (red channel only). **(e)** Vesicle showing axially symmetric ring domains. **(f)** Equatorial section of a vesicle similar to **(a)**. **(b)** **(c)** **(f)** are equatorial section, while **(a)** **(e)** hemispherical projections of image stacks taken at $0.5\mu m$ spacing. Scale bars are $5\mu m$. Figure adapted from [4].

for the lipid bilayer than for water, v decreases with increasing temperature. Changes in osmotic pressure causes the inflation or deflation of the vesicle, therefore respectively increasing or decreasing v [48].

2.4 Inducing curvature on ternary membranes

The difference in bending modulus of the two phases (L_o and L_d) causes an immediate consequence. Locally bending a liquid-liquid phase-separated bilayer requires the payment of an energy toll that would be lower if the L_d phase were the one with the highest curvature. Therefore one may expect that a locally bent ternary membrane, evolving through the diffusion of lipid molecules and domains in order to minimise its free energy, would naturally

end up with L_o domains placed on flat (or less curved) areas, and L_d domains on the most curved ones. This effect has been described in [4], where phase-separated GUVs were observed in different conditions with two-photon microscopy, which allowed the high resolution of Figure 2.5. Many groups also investigated this aspect using different techniques to induce a local curvature in the lipid bilayer. In [59] and [75] for example the curvature-induced sorting of lipids is inspected using a double bilayer system. This method consists in the deposition via vesicle rupture of a first supported lipid bilayer of uniform composition on a micropatterned surface, followed by another deposition, again via vesicle rupture, of the DPPC/DOPC/Cholesterol bilayer. The vesicle rupture method ensures a thorough mixing of the lipids, that partition again in the two phases once the bilayer is formed. Both works confirm the presence of L_d domains in correspondence of the high-curvature features, whereas the L_o phase prefers flat areas.

My work studies instead the effect of locally induced high curvature in a ternary Giant Unilamellar Vesicle, pressed by buoyancy against a silicone surface structured by micrometric spherical caps. Because of the difference in bending modulus between the two phases, and since L_d domains diffuse across the membrane [10], one would expect to see L_d domains placing preferably on high-curvature areas of the membrane, leaving the flat regions to the stiffer L_o phase. This phenomenon would manifest itself as L_d domains casually arriving on the PDMS features during their diffusion motion and not leaving them, the PDMS features acting as traps associated with an energy barrier.

2.5 Simple estimates of membrane bending on topographically patterned surfaces

It is already possible to estimate the order of magnitude of the trapping effect from geometric considerations only, assuming that there are no specific interactions between the silicone surface and the membrane.

The vesicle being pressed against the surface by buoyancy, it is reasonable to assume that the membrane would follow the surface of the bump, and then be slightly lifted to smooth the transition to the flat region. Therefore I modelled the surface in proximity to a bump as a spherical cap stitched to a surface of revolution generated by a catenary (see Figure 2.6). The ana-

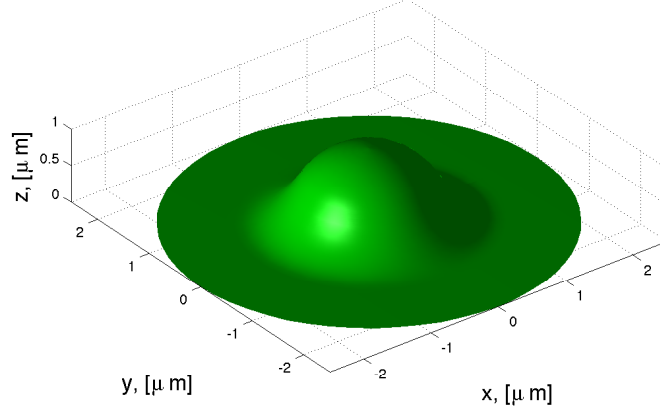


Figure 2.6 – 3D model of the deformation induced by the PDMS features on the membrane.

lytical expression employed to model the deformed membrane allowed me to calculate its bending energy using equations (2.3.4) and (2.3.5). Experimental values for the bending moduli of the two phases were taken from [89] ($\sim 100kT$ and $\sim 45kT$ for the L_o and L_d phase respectively). For a radius of deformation (defined as the furthest distance from the centre of the bump at which the membrane is still not flat) of $2.6\mu m$ the bending energy is at its minimum value, that is $\sim 700kT$ and $\sim 300kT$ for the L_o and L_d phase respectively. It is possible to extract two interesting informations from these estimates.

First, the energy toll required for bending the membrane is two order of magnitude smaller than the potential energy of the vesicle floating at $1\mu m$ (the radius r of the features) from the silicone surface, that we can evaluate as $\frac{4}{3}\pi R^3 \Delta\rho g r \approx 2.4 \times 10^{-16} J \approx 6 \times 10^4 kT$ (where R is the radius of the vesicle, roughly $60\mu m$, and $\Delta\rho$ the density mismatch between the solution that fills the vesicle and the outer medium). Therefore there is no doubt that the membrane will bend in proximity of the high-curvature features.

Second, there is an important energy gain ($\sim 400kT$) for a membrane having the L_d phase deformed in lieu of the L_o one, although the value obtained with this calculation may be overestimated for small domains. For L_d domains with a smaller radius than the one employed in the calculations the surrounding L_o phase is likely to be at least slightly bent, therefore increasing the bending energy. The results of my experimental work are in agreement with this result.

Chapter 3

Materials and experimental methods

3.1 Soft Lithography

The term “soft lithography” refers to a family of techniques for fabricating or replicating structures using soft, elastomeric elements in pattern formation [65]. Soft lithography on poly(dimethylsiloxane) (PDMS) was used in this work to prepare a substrate with micrometrical features. PDMS is broadly used in soft lithography because it is easy and fast to work with, and ensures a nanoscale precision in making replica of a mould [87].

3.1.1 Poly(dimethylsiloxane) chemistry

Poly(dimethylsiloxane) (PDMS) is a silicon-based organic polymer. It is composed by a chain of repeating $[\text{Si}(\text{CH}_3)_2\text{O}]$ monomeric units terminated at both ends by a silicon atom with three methyl groups attached, thus making the formula $\text{CH}_3[\text{Si}(\text{CH}_3)_2\text{O}]_n\text{Si}(\text{CH}_3)_3$ (see Figure 3.1). The PDMS can be cured by forming $\text{Si}-\text{CH}_2-\text{CH}_2-\text{Si}$ bonds in multiple sites and between different chains, therefore creating a 3D cross-linked structure. After the cure the PDMS is solid, elastic, and optically clear.

The silicone used in this work was the Sylgard® 184 by Dow Corning, which is a standard in soft lithography. It is a PDMS elastomer cured as written above, using a proprietary platinum-based catalyst.

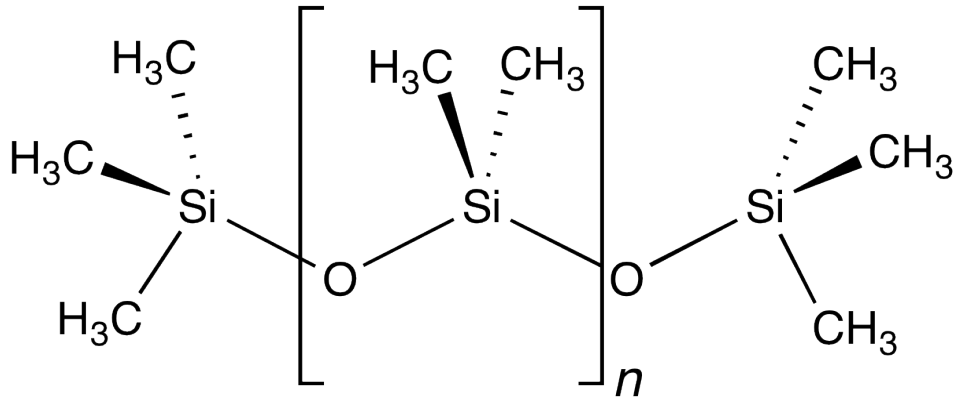


Figure 3.1 – PDMS chemical structure.

3.1.2 Surface preparation protocol

The protocol used to prepare the PDMS surface can be divided in two parts. In the first part (Figure 3.2), that ends with the production of a PDMS master, [75] was closely followed, although with some variations. This part of the protocol was also inspired by the soft lithography techniques described in [60, 8, 61]. In the second part, the PDMS double casting, [25] was followed (see Figure 3.3).

Firstly, 2 μ m diameter Sulphate-modified Polystyrene (PS) microsphere from Invitrogen (8.1% solid volume) were diluted 1:10 with ultra-pure water in an eppendorf tube. The suspension was then centrifuged so that the colloids deposited at the bottom of the eppendorf, and the water was changed with new ultra-pure water. This procedure was performed three times, to clean the colloidal suspension. The clean suspension was then stored in glass vials in a refrigerator. Aliquots were then taken from the vial and diluted again with ultra-pure water and isopropanol (in a 2:4:4 proportion) in an eppendorf tube.

The PDMS was prepared by thoroughly mixing the two components of the Sylgard® 184 kit (base and curing agent) in a 10:1 proportion in a clean plastic cup. The plastic cup was then covered with pierced parafilm and put in vacuum for half an hour, in order to degas the PDMS (the parafilm was needed to minimise contamination, e.g. by dust carried by air entering the desiccator at the end of the degassing).

A 35mm Petri dish (by Cellstar) was filled halfway to the top with ultra-pure water (18.2M Ω cm resistivity). Next, the colloidal suspension in water

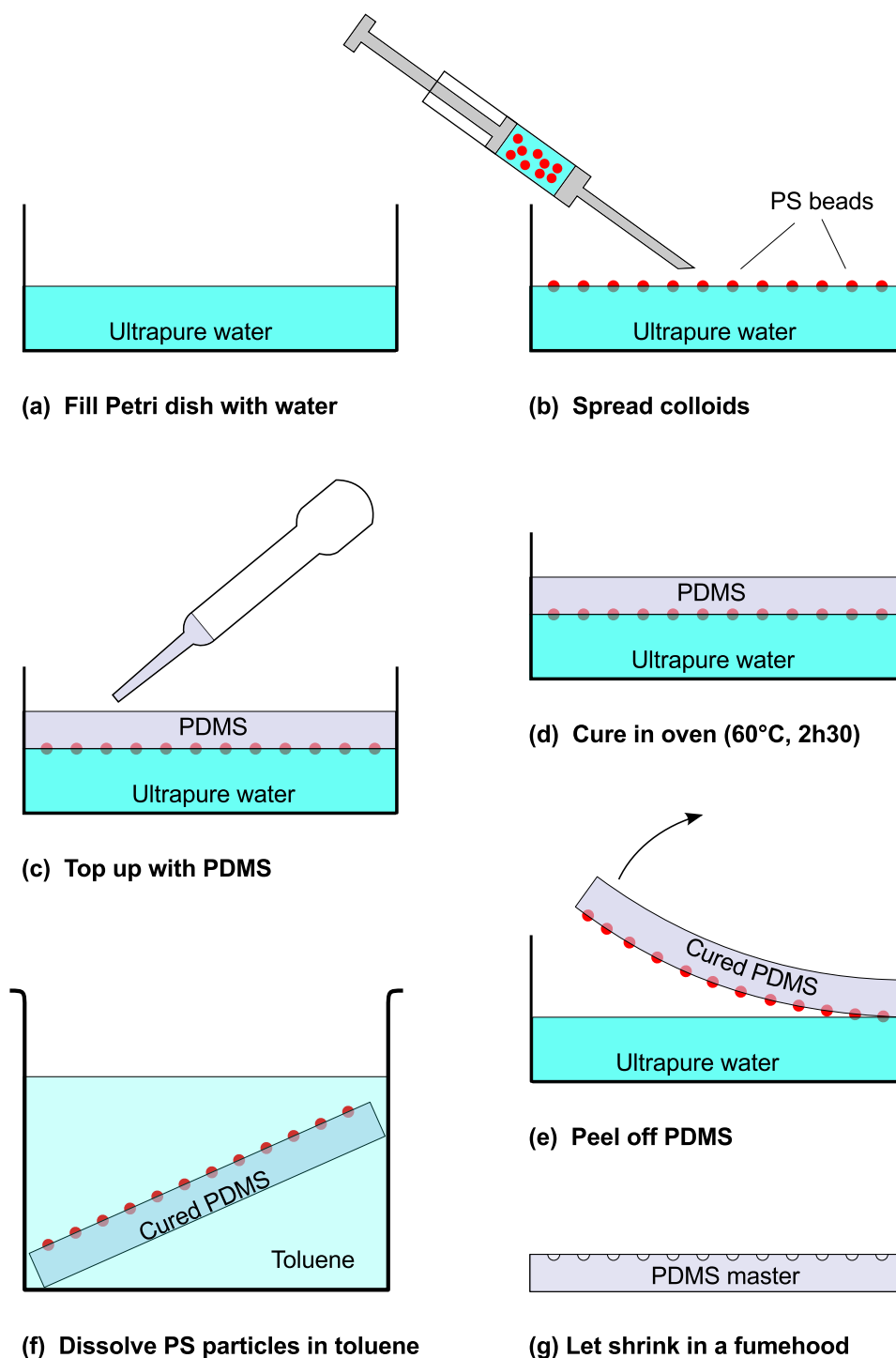


Figure 3.2 – PDMS master preparation. Soft lithography technique for the preparation of the PDMS mould. (a) A Petri dish is filled halfway to the top with ultrapure water. (b) Polystyrene beads are spread at the air/water interface using a microsyringe. (c) A layer of PDMS is spread on top of the colloids. (d) The Petri dish is left in an oven for the PDMS to cure. (e) The cured PDMS is solid, and it embeds the colloids as it is peeled off the water surface. (f) The cured PDMS is soaked in toluene to dissolve the PS beads, and (g) left to shrink under a fume hood.

and isopropanol (IPA) was spread drop-wise at the air-water interface using a 50 μ l microsyringe. A couple of minutes were then waited, so that the IPA could evaporate, leaving the PS beads trapped at the air-water interface [63].

The PDMS was then carefully spread on the water surface using a disposable plastic pipette, trying to make a layer as even as possible (this was hindered by the high cohesion of the PDMS). The PDMS was then cured by placing the Petri dish in an oven at 60 °C for 2.5h, so that the colloids became embedded in the PDMS layer.

After the curing process, the PDMS was lifted from the water surface and soaked in a beaker with toluene for 6h, in order to dissolve the PS particles while leaving the PDMS intact. Since the PDMS swells dramatically in toluene, it was necessary to leave it shrinking overnight in an empty beaker under a fume cupboard. The result of this procedure is a PDMS cylinder with a flat surface with 1 μ m radius hemispherical holes, suitable to be used as a mould in the double-casting process.

The mould was then placed on the bottom of an empty 35mm Petri dish, with the patterned surface facing up, and subjected to a silanisation process. Five moulds were placed in a glass desiccator and four 40 μ l drops of 1H,1H,2H,2H-per-fluorodecyltrichlorosilane were placed on aluminium trays arranged symmetrically at the edges of the desiccator. A vacuum pump was then connected to the desiccator and left running for 2 minutes, after which the valve of the desiccator was closed. The moulds were kept under vacuum in a silane atmosphere for 1.5h before being removed from the desiccator. The effect of the silanisation process is the absorption, self-assembly and covalent bonding (through $-Si-O-Si-$ bonds) of silane molecules on the PDMS surface, resulting in a densely packed self-assembled monolayer necessary to achieve a non-adhesive behaviour of the PDMS surface [25, 45].

Next, uncured PDMS was cast on the silanised mould and cured at 60°C for 2.5h. The new PDMS layer was then peeled away from the mould in order to obtain a negative replica of the mould, i.e. a flat surface with hemispherical 1 μ m radius features (“bumps”).

The PDMS substrates were stored in parafilm sealed Petri dishes.

While the procedure could have been stopped right after the first step in order to obtain micrometric features on the surface, the double-casting technique was employed to obtain a chemically homogeneous patterned surface, which was deemed preferable.

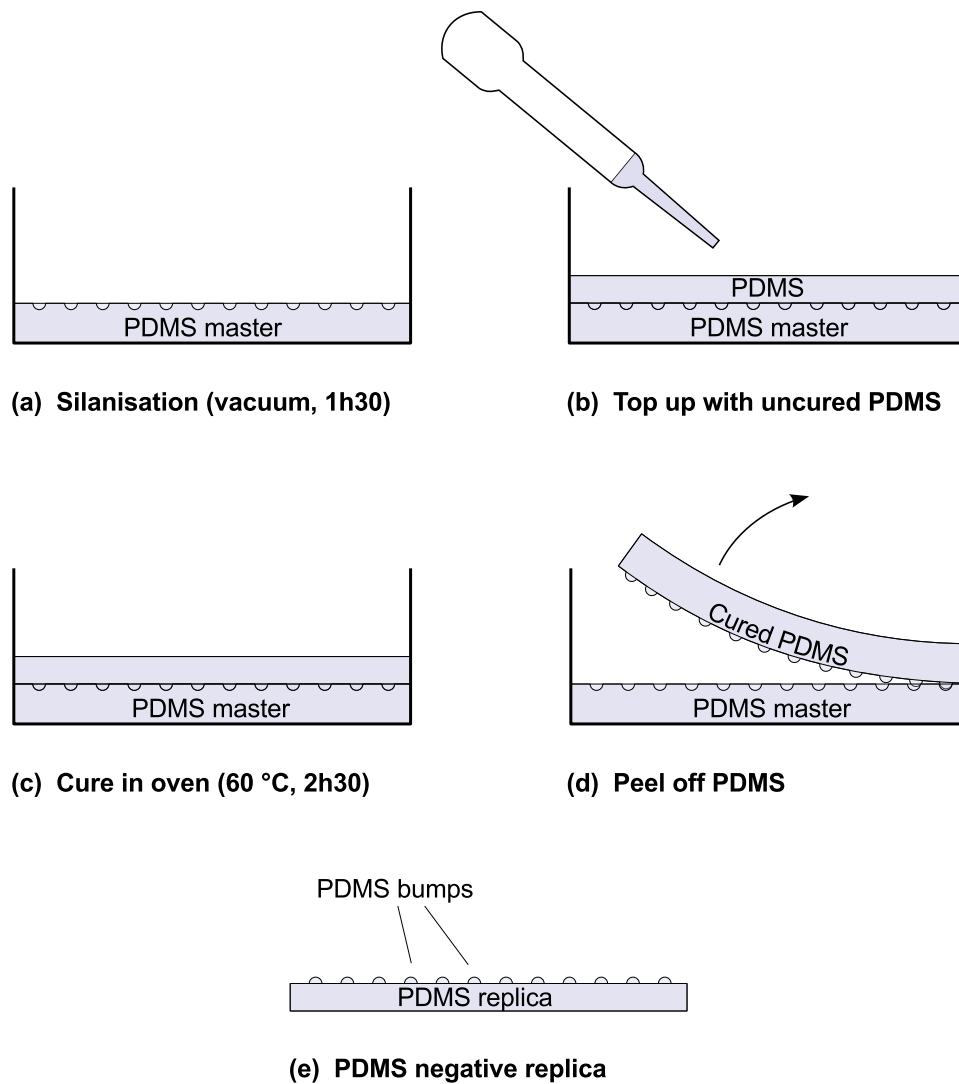


Figure 3.3 – PDMS double-casting. (a) The PDMS mould is silanised via vapour deposition, then (b) new PDMS is cast and (c) cured. When solid it is peeled away (d) from the mould, resulting in (e), a negative replica of the mould (therefore a flat surface with protruding features).

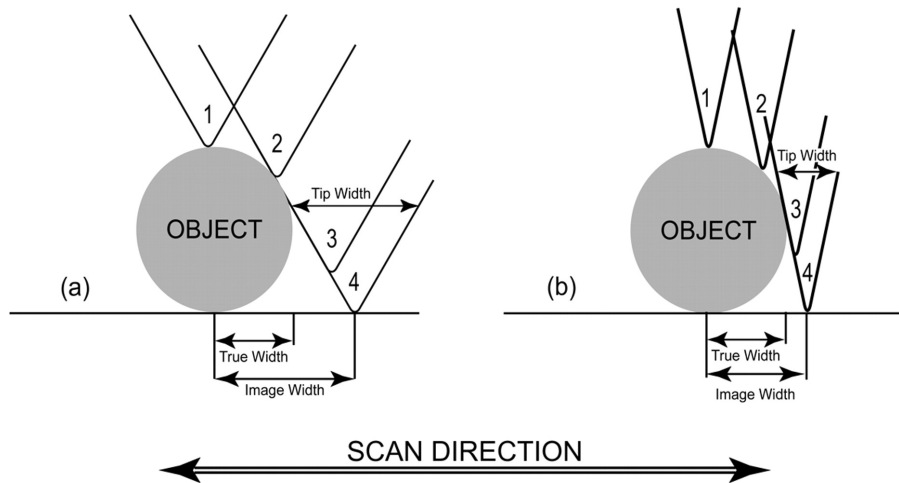


Figure 3.4 – AFM: tip-sample convolution. Example of tip-sample convolution in Atomic Force Microscopy: due to the pyramidal shape of the tip, the recorded image does not reproduce carefully the sample. Image adapted from [42].

3.1.3 Surface characterisation

The preparation process of the patterned surface was monitored with different techniques. The proper spreading of the colloids at the air-water interface was checked using an optical microscope (Zeiss Axioplan) while more sophisticated instruments were employed to assess the subsequent stages.

Two microscopy techniques have been used to characterise the final PDMS patterned surface: Scanning Electron Microscopy (SEM) and Atomic Force Microscopy (AFM). These two techniques have been chosen because they compensate each other's weaknesses, their combination allowing to overcome the limits of the single techniques.

The AFM is very accurate in the assessment of the profile of a sample, being very precise in the vertical direction. However, its resolution in the xy plane is limited by the physical dimensions of the probe. Any AFM image is actually the convolution of the true shape of the studied object and the shape of the probe, making protruding objects appear wider. This problem is particularly severe when dealing with surfaces with important roughness, and represents one of the biggest limitations to the use of AFM as it can not be solved entirely: it is possible to deconvolve the AFM image and the shape of the tip, but some information can not be retrieved (see Figure 3.4).

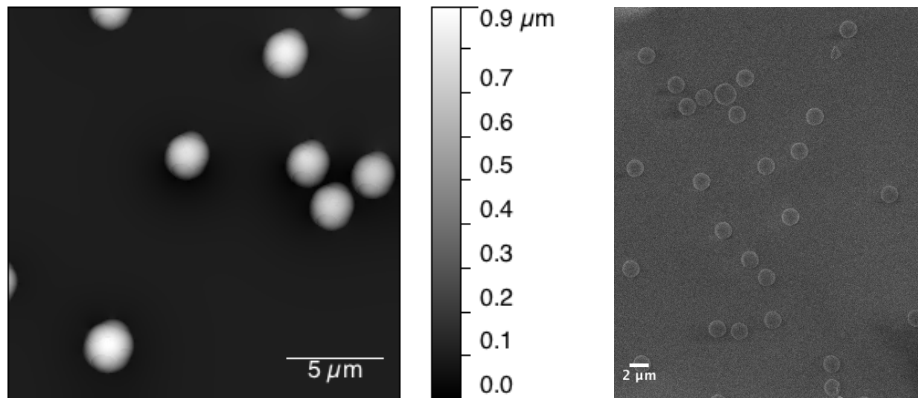


Figure 3.5 – AFM and SEM images of the PDMS surface. (left) AFM scan, taken in non-contact mode, of the PDMS patterned surface. (right) SEM image of a different portion of the same sample.

On the other hand a Scanning Electron Microscope offers very resolved plan views of the samples, but estimates of height with this technique are always indirect and subject to possible artefacts (e.g. freeze-fracture shadow-casting combined with cryo-SEM imaging, see [34]).

The combination of the two techniques allows then to assess both the height and the lateral dimensions of the features of the PDMS surface.

AFM measurements of PDMS bumps were done with a XE-100 by Park Systems in non-contact mode, using a Si probe (910M-NCHR, working at 317kHz). A different measurement, on PS colloids embedded in the PDMS surface (at stage (e) of Figure 3.2) was performed in contact mode using an AFM by NanoWizard II equipped with a PNP-TR-20 Silicon Nitride probe by Nano World. The diameter of the PDMS bumps was measured instead analysing SEM images (taken with a Supra™ 40 by Zeiss, equipped with InLens detector, and operated with an incident beam of energy $2keV$).

The height of the bumps resulted to be $0.74 \pm 0.02 \mu m$, while the diameter $1.78 \pm 0.01 \mu m$ (see Figure 3.5). This, together with the value obtained for the height of PS colloids from the PDMS surface ($1.1 \pm 0.02 \mu m$), seems to suggest that the colloids employed were actually slightly smaller ($0.9 \mu m$ in radius) than the nominal value. It is worth to point out, although it is unlikely, that the silanisation process may have caused a backfilling of the holes left by the dissolution of the colloids [76], leading to an underestimate of the radius of the colloids.

3.2 Giant Unilamellar Vesicles

Different techniques are available to produce artificial lipid bilayers. According to which technique is employed different types of lipid bilayer will be obtained: flat bilayers or vesicles [32, 53]. In this work Giant Unilamellar Vesicles (GUVs, defined as ranging from $5\mu\text{m}$ to $200\mu\text{m}$ in radius) were employed. The analysis actually focused only on GUVs with radius larger than $55\mu\text{m}$ and smaller than $120\mu\text{m}$ (the upper limit being a physical constraint due to the size of the imaging chamber, the problem will be addressed in section 3.2.3).

GUVs were chosen since they had been shown to be a nice (and relatively simple to reproduce) experimental system presenting liquid-liquid phase separation [81, 82].

3.2.1 Ternary lipid mixture

Various different lipid compositions have been used to achieve a liquid-liquid phase separated membrane. The majority of them is very similar, being composed by a sterol and two different phospholipids, one with high melting temperature (T_m), one with a low one.

In this work a mixture of diPhyPC (1,2-diphytanoyl-sn-glycero-3-phosphocholine), DPPC (1,2-dipalmitoyl-sn-glycero-3-phosphocholine) and dihydro-cholesterol (dChol, also known as cholestanol) was used. The phospholipids were supplied by Avanti Polar Lipids (Alabaster, AL), while the cholestanol was from Sigma. DPPC is the high T_m component in the mixture ($41\text{ }^\circ\text{C}$) [71], while diPhyPC has a really low T_m ($< -120\text{ }^\circ\text{C}$) [47]. Such a low T_m is only due to the presence of numerous methyl groups branching from the acyl tails, acting as a steric hindrance and preventing the close packing of the lipid molecules, therefore reducing T_m [47].

This particular lipid mixture has been chosen because it is suitable for imaging [80]. It is very similar to the diPhyPC/DPPC/cholesterol mixture that has recently been used in many works [80, 89, 30, 31]. Both these two mixtures present liquid-liquid phase separation for a wide range of lipid composition, and both employ only saturated phospholipids. This prevents the risk for the lipids to undergo photooxidation, phenomenon which is known to alter the physical properties of the bilayer [80, 3]. Preventing photooxidation is also the reason why cholesterol was replaced by cholestanol, its saturated

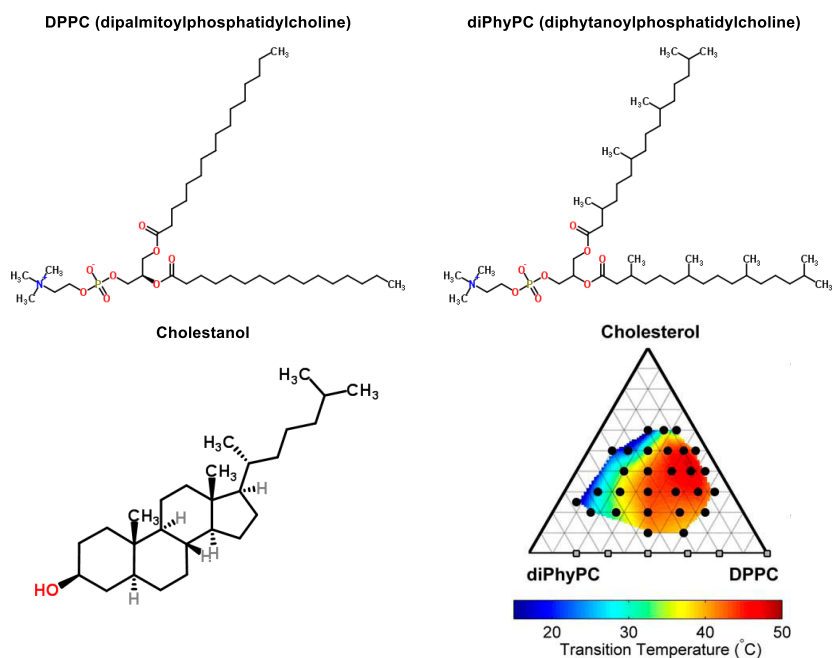


Figure 3.6 – Chemical structures of the lipids used in this work, and phase diagram from the literature. (top, left) Structure of the DPPC, employed as the high- T_m lipid in the ternary lipid mixture. **(top, right)** Structure of the diPhyPC, low- T_m lipid. Methyl groups branching out of the acyl chains are visible. Said groups act as steric hindrance, therefore impeding the close-packing of the lipid molecules. **(bottom, left)** Structure of the cholestanol (also known as dihydro-cholesterol), saturated form of cholesterol. **(bottom, right)** Taken from [80]. Diagram, determined by fluorescence microscopy, of the phase behaviour of vesicles composed of DPPC, diPhyPC and cholesterol. Black circles denote compositions exhibiting coexisting liquid phases, grey squares denote gel-liquid coexistence, observed in membranes without cholesterol. Miscibility transition temperature is shown by the colour scale. Although the lipid mixture employed in this work was slightly different, its behaviour is expected to be qualitatively similar.

version. This of course caused the phase diagram of the composition to be slightly different from the one in [80] and reported in Figure 3.6.

The use of the diPhyPC/DPPC/cholestanol mixture yielded phase-separated GUVs, in which the L_o phase was enriched in DPPC (high T_m) and cholesterol, while the L_d phase was mainly composed of diPhyPC (low T_m) [80]. In order to tell apart the two phases 0.8% mol of Texas Red labelled DPPC (Texas Red DHPE, by Invitrogen) were added to the mixture. The dye is attached to the headgroup of the lipid, and causes the lipid to behave differently than the standard DPPC: due to the extra volume, the DHPE partitions preferably in the L_d phase [83]. The concentration of Texas Red DHPE was chosen knowing that this particular lipid doesn't affect significantly crucial properties of the bilayer, such as the phase transition temperature, even in concentrations of 2% mol [82] (unlike other dyes [22, 51, 66]).

DiPhyPC, DPPC and cholesterol were mixed in a proportion of 27:27:45 mol fraction (plus 0.8% mol Texas Red DHPE), ensuring GUVs with a similar proportion of L_o and L_d phase and a transition temperature slightly above room temperature. This turned out to be useful when the need of re-mixing phase separated vesicles showed up, shortening the time needed for their heating.

3.2.2 Electroformation protocol

The GUVs used in this work were prepared by electroformation, a standard technique that relies on the hydration of dry lipid film in an oscillating electric field. The protocol used is closely related to [83].

The ternary lipid composition was deposited on an Indium Tin Oxide (ITO) coated slide, provided by Visiontek Systems Ltd, that had previously been cleaned by sonication in ultra-pure water and IPA. The deposition and spreading, being performed by hand, was the least reproducible part of this protocol, hence great care has been taken to replicate the procedure. Both the ITO coated slide and the lipid composition were heated to 60 °C, a 30µl drop of lipid composition was deposited at the centre of the slide, and the spreading was performed with the help of a clean coverslip, in two slow strokes (from the centre to a side and back to the centre) without lifting the coverslip. If performed correctly, this ensured an even spreading of the lipid film, that resulted in a composition of the GUVs very similar to the starting

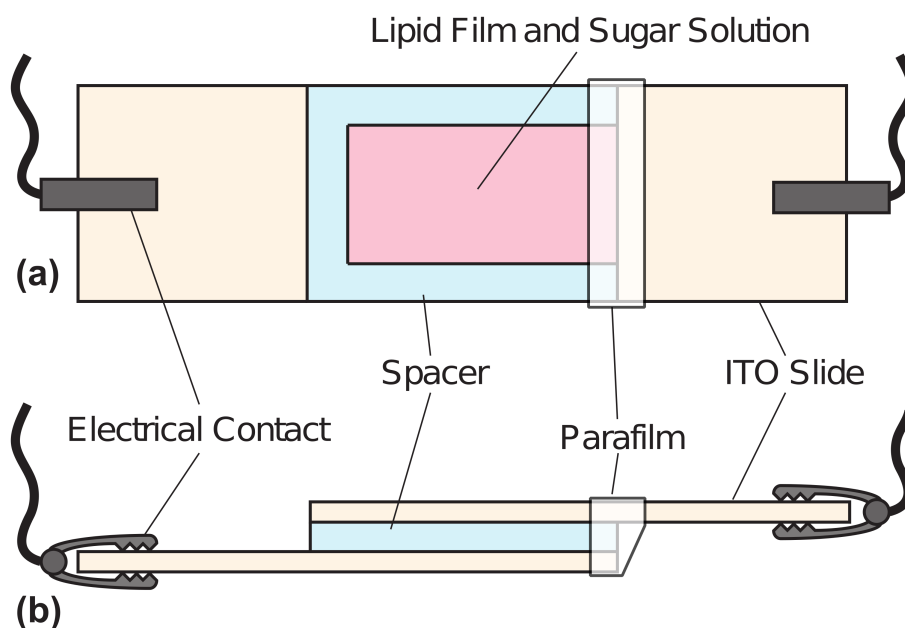


Figure 3.7 – Diagram of the electroformation chamber. Schematic representation of the electroformation chamber viewed from the top (a) and from the side (b). Adapted from [23].

mixture.

The slide was then placed in vacuum for at least an hour, to remove any solvent residue. Using a 0.5mm thick U-shaped spacer (cut from a sheet of Altec AlteSil), the lipid coated slide and another, clean, ITO coated slide an electroformation chamber was assembled, as schematically shown in Figure 3.7.

The conductive slides were faced inwards and slightly shifted, separated by the U-shaped spacer that seals three sides of the chamber. The chamber was then filled with the swelling solution, a degassed and filtered ($0.22\mu\text{m}$) glucose (from Sigma-Aldrich) solution in ultrapure water (200mMol), and sealed with parafilm. Binder clips were employed to make sure that the chamber held together.

Finally, the chamber was connected by two alligator clips to a function generator that provided a sinusoidal signal with 1V peak-to-peak amplitude and 10 Hz frequency. The signal was applied for 1 hour, during which the chamber was heated at $60\text{ }^\circ\text{C}$, to enhance the mixing of the different lip-

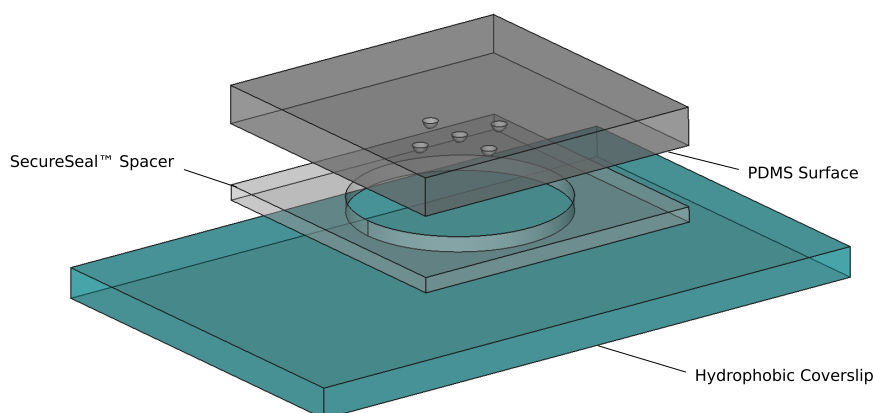


Figure 3.8 – Diagram of the imaging chamber. The bumps on the PDMS surface are shown just for display purpose: they are neither visible to the naked eye nor arranged in an ordered pattern.

ids. This protocol produced a great number of GUVs with a broad radius distribution, typically between 10 and 100 μm .

After the electroformation the GUVs were stored in plastic eppendorf tubes in the dark until the imaging, that was always performed within 4 days.

3.2.3 Sample chamber

Prior to the imaging the GUVs were suspended again in a filtered and degassed sucrose solution with same osmolarity (197 mMol, from Sigma-Aldrich), usually in a 1:9 ratio.

A SecureSeal™ circular spacer (from Grace Bio-Labs, 9mm diameter, 120 μm thickness) was placed on a coverslip, and the resulting well was filled with the GUV suspension. The chamber was then sealed with the PDMS patterned surface placed on top, as schematically shown in Figure 3.8. The coverslip used was a hydrophobic one (provided by Trevigen), expressly chosen to hinder the formation of leaks from the imaging chamber.

The buoyancy arising from the density mismatch between the glucose solution filling the GUVs and the sucrose solution in the outer medium caused the vesicles to float and press against the patterned PDMS surface, creating a semi-supported bilayer. The lipid bilayer of the GUV follows the topography

of the surface, therefore being forced by the micrometric features to take a controlled, high curvature.

Unfortunately, the size of the sample chamber was a constraint for the size of the GUVs that could have been observed. Any GUV significantly bigger than $120\mu\text{m}$ in diameter (the thickness of the spacer) would have exploded, being pressed between the coverslip on the bottom of the chamber and the PDMS on top.

3.2.4 Epifluorescence microscopy

The imaging of the GUVs, labelled with Texas Red DHPE, was achieved through epifluorescence. A Nikon Ti-E inverted microscope (imaging from below) equipped with a 40x dry Nikon objective was employed, the light source being a mercury lamp with a Texas Red filter (by Semrock). The image sequences were acquired using a digital camera provided by Ximea (either the MQ013MG-E2 or the MQ013RG-E2) and digitally recorded on a linux workstation running a custom video grabbing program developed in the lab (Dr Jurij Kotar). Using the 40x dry objective (NA 0.75), the pixel size was 131.6 nm for both cameras. The frame rate was set to 20 fps, that would have yielded an exposure time of 50 ms. However, when the actual time stamps of the frames were read, the exposure time turned out to be slightly smaller (48.7 ms, corresponding to a 20.53 fps frame rate).

The focal plan was at the region where the GUV's membrane flattened against the PDMS patterned surface. The PDMS features in contact with the GUV were imaged in bright field, few seconds after the end of the acquisition of the epifluorescence video of the GUV. All image sequences were acquired at room temperature (23 °C).

Chapter 4

Analysis and results

As discussed in sections 2.3 and 2.4, the two liquid phases L_d and L_o are characterised by different bending moduli, making it energetically favourable for a lipid bilayer with locally forced curvature to laterally organise so that L_d domains are placed in correspondence of high curvature points. But diffusion of L_d domains in the GUV membrane has been found to be Brownian on short timescale [10], after which effects of the presence of neighbouring domains can be seen [70, 33]. These two aspects suggested that in the system studied in this work domains would diffuse until they happened to be placed on a bump, that would then act as a trap confining their motion. Our expectation is that a L_d domain placing himself in correspondence of a bump would significantly lower the energy toll that the bump-induced curvature takes, therefore it would be energetically inconvenient for it to move away from the high-curvature spot.

Thus, the behaviour of the semi-supported membrane showing liquid-liquid phase-coexistence was investigated through the analysis of the Mean Square Displacement (MSD) of the L_d domains across the L_o continuous phase.

Data analysis, when not stated otherwise, was carried on using MatLab code developed ad-hoc.

4.1 Tracking

The first step in data analysis is the tracking of the L_d domains in the L_o phase. The L_d domains are brighter than the L_o continuous phase, because, as mentioned in section 3.2.1 the fluorescent dye partitions in the L_d phase.

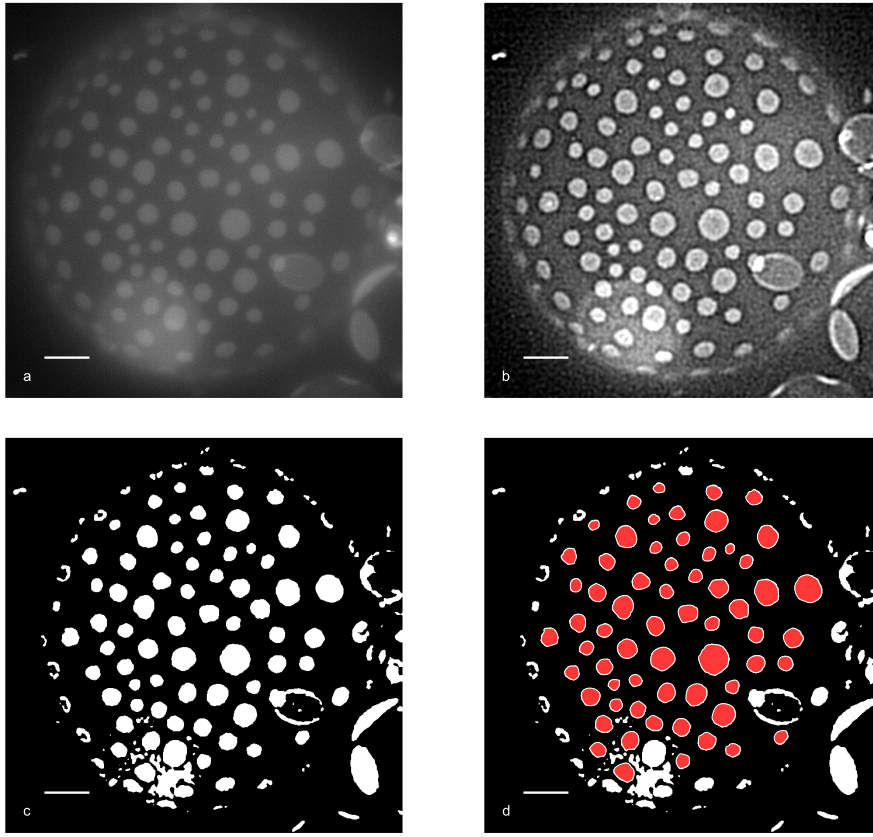


Figure 4.1 – Filtering and feature-recognition. (a) Original, 16bit grey-scale frame. (b) Same frame, after the bandpass Fourier filter was applied. (c) Thresholded frame. (d) Detected domains. Scale bars are $10\mu m$.

Every 16 bit grayscale frame is therefore treated with a 2D bandpass Fourier filter (a difference of gaussians) and thresholded, in order to obtain a binary image (see Figure 4.1). Connected white regions are then detected and, using a function (from the Image Processing Toolbox in Matlab) that exploit their properties, some of them are identified as L_d domains. To be identified as domains, connected regions have to be approximately circular (domains in coexisting liquid-liquid phases are supposed to), with a surface area ranging from $40px^2$ ($\sim 0.7\mu m^2$, to avoid any noise that survived the bandpass filter) to $3000px^2$ ($\sim 52\mu m^2$). This upper limit was set to avoid to track small vesicles floating inside the observed GUV as if they were domains.

The positions of the domains are determined from their centroids (i.e. center-of-mass, with mass corresponding to pixel intensity), the diameters

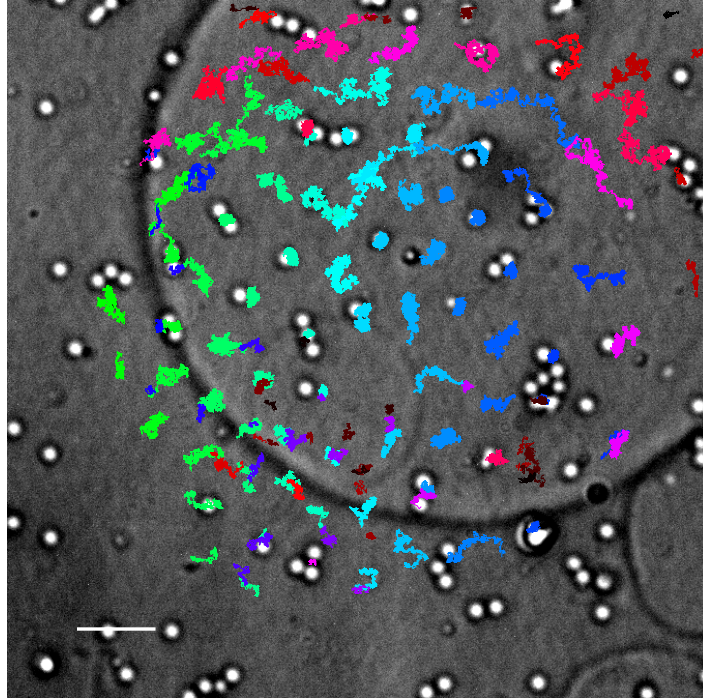


Figure 4.2 – Tracking of domains, showing pinning on the bumps. L_d domains trajectories, superposed on a bright field image of the PDMS surface. The colours are in order of detection: green trajectories belong to domains detected early during the video, red ones were the last ones detected. Reasons for different domains being detected for the first time at different frames are diffusion, rolling of the GUV, and coalescing. In the former two cases the domains are detected as soon as they appear in the video. Instead, when two domains coalesce into one, this is seen as a totally new domain, therefore its trajectory starts at the coalescence time. The bright field image of the PDMS surface, in which the micrometric features appear as bright spots with a darker outline, is taken at the end of the epifluorescence video. The big, dark circles are profiles of vesicles. The biggest one is the analysed GUV, while the smaller two in the bottom right corner just happened to be in the field of view of the microscope, but were not analysed. The outline of the GUV in the bright field image doesn't enclose all the trajectories of the domains because the GUV drifted during the imaging. Scale bar is $10\mu m$.

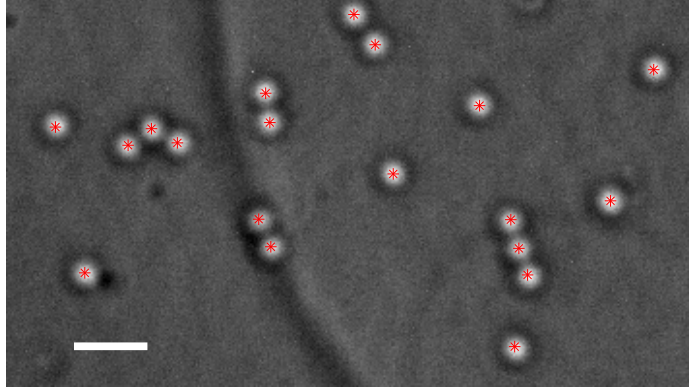


Figure 4.3 – PDMS features ("bumps") location. Detail of a bright field image of the PDMS surface, with the micrometric bumps marked by the features-locating script. Scale bar is $5\mu m$.

from the average between short and long axis of the approximating ellipse.

The positions of the domains are then compared with the positions found at the previous frames, in order to link each domain to the right trajectory (each domain is matched with the nearest features in the previous image, and if no preexisting trajectories are found close to a domain this is considered as new).

The control on the eccentricity of domains automatically discriminates coalescing domains: when two domains unite, their individual trajectories end, and when the resulting domain equilibrates in a round shape a new trajectory begins.

Since there is no tracking of the actual GUV, the tracking script so far saves the positions of all round objects whose diameter falls within a certain range. Thus these round objects can be totally unconnected with the GUV, for example they could be small vesicles that floated in the field of view of the camera. Therefore before proceeding to the analysis of the trajectories a control step is needed, in which all trajectories that are suspected not to belong to a L_d domain are manually deleted.

4.1.1 Features location

The bumps on the PDMS surface are located submitting the bright field image taken at the end of the imaging with epifluorescence to a peak-finding function, that returns local maxima positions with a sub-pixel precision (see Figure 4.3).

4.2 Mean Square Displacement analysis

In order to assess the influence that the PDMS features yields through the high curvature they force on the bilayer, each trajectory is split in several short “sub-trajectories”, each 20 frames long. These sub-trajectories are then treated as if they belonged to different domains, and $MSD(\tau)$ is calculated for each of them.

Each of the aforementioned subtrajectories is then compared with the location of the PDMS bumps. If the distance between the centre of the domain and the closest bump ever falls below the radius of the domain, the subtrajectory is flagged as “on a bump” (see Figure 4.4).

The expedient of splitting the trajectories is equivalent to splitting the video in several 20-frames-long segments and analysing them separately, and it is essential for the analysis. For example, let us assume that a L_d domains diffuses freely for half the imaging time, and then places itself on a bump. The simple calculation of its MSD from its trajectory over the entire imaging time would average on the two (supposedly different) behaviours, therefore making it very difficult to draw any conclusion. With this expedient instead the two behaviours are analysed separately.

From Figure 4.4 it is already possible to see the effect of the bending modulus difference, since some domains seem to get pinned by the PDMS bumps, not moving away from them for the entire imaging time.

4.2.1 Mean Square Displacement calculation

The Mean Square Displacement is calculated for each of the subtrajectories as

$$MSD_i(\tau) = \frac{1}{t_{tot} - \tau} \sum_{t=0}^{t_{tot}-\tau} (r_i(t + \tau) - r_i(t))^2, \quad (4.2.1)$$

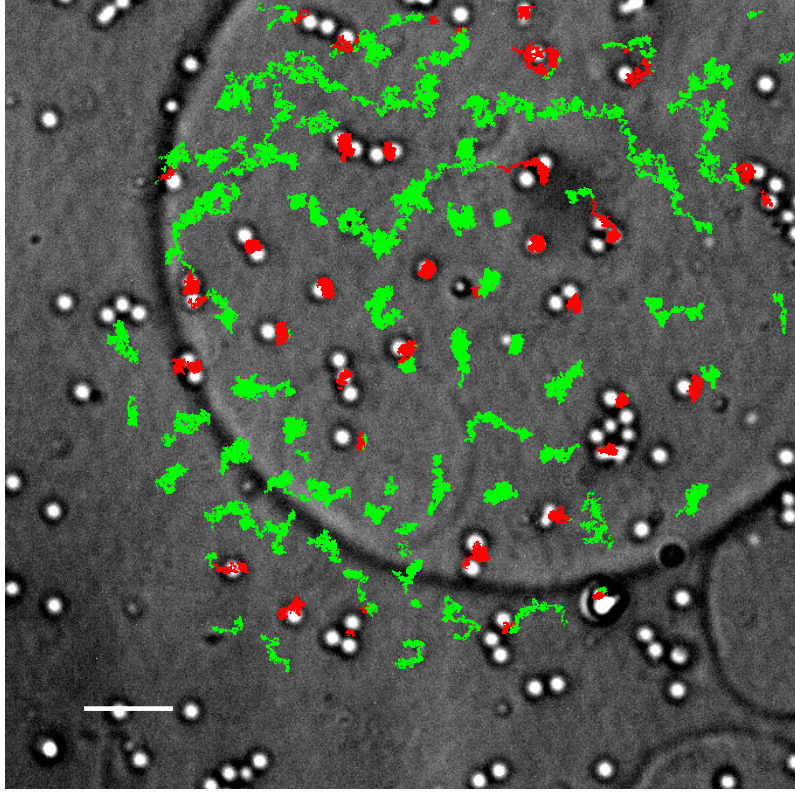


Figure 4.4 – L_d domains getting stuck on bumps. Trajectories of the domains superposed to the bright field image of the PDMS surface. The sections of the trajectories flagged as “on a bump” are displayed in red. Scale bar is $10\mu m$

where t_{tot} is the total time of each subtrajectory, r_i the array of positions (i.e. the i -th subtrajectory), τ the lag time.

The distribution of the MSDs is then plotted, at fixed lag times (see Figure 4.5). This distribution, that turns out to be lognormal, gives statistics both on different domains and on the history of the single domain.

In order to calculate the diffusion coefficients, I found it more reliable to limit the calculation to the early times, because in this case the motion is less affected by possible caging effects. Therefore only the first 5 points of the MSD were fitted, where the squared displacement is linear with the lag time, and the usual relation for Brownian motion in 2D holds:

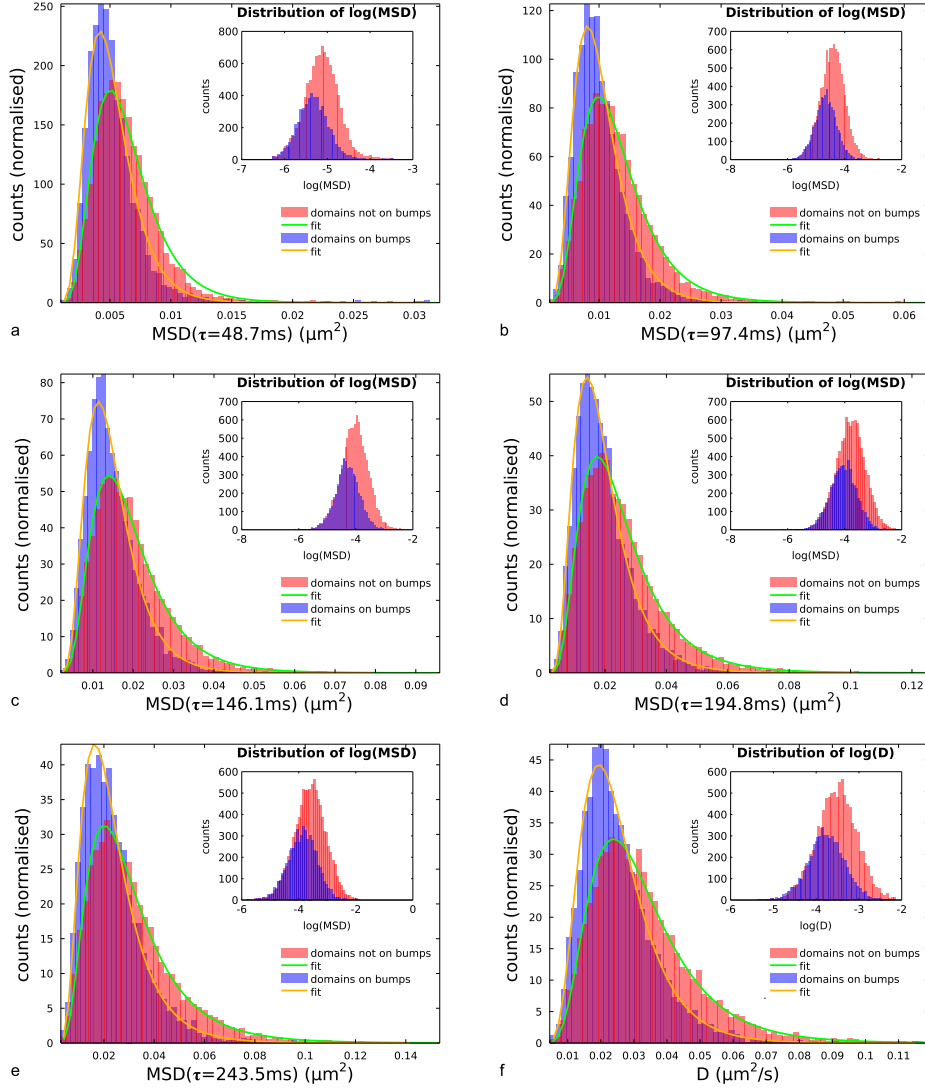


Figure 4.5 – Distribution of the Mean Square Displacement and of the diffusion coefficient, showing the different behaviour of L_d domains on bumps and not on bumps. (a-e) Histograms of MSD at different lag times, and (f) of the diffusion coefficient. Data have been found to follow a lognormal distribution, as shown by the fit (lines) and (insets) by the histograms of the natural logarithm of the data, that follow a gaussian distribution. Aside from the insets, histograms have been normalised to have unit area.

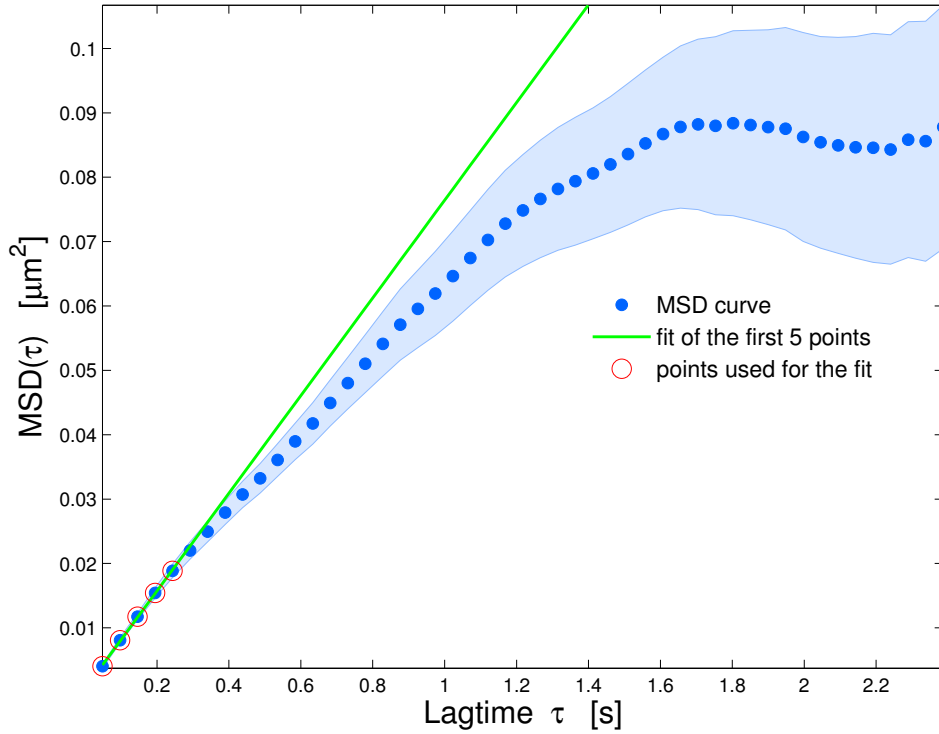


Figure 4.6 – Example of MSD curve. Mean Squared Displacement curve of a L_d domain, plotted against the lag time. The green line is the fit of the first few (5) points of the curve (in red). Its angular coefficient, divided by 4, is the diffusion coefficient of the domain (see equation (4.2.2)). For longer lag times, the curve deviates from a linear behaviour, suggesting that the motion of the L_d domain is not Brownian, but somehow confined.

$$MSD_i(\tau) = 4D_i\tau. \quad (4.2.2)$$

Equation (4.2.2) is employed for subtrajectories “on a bump” as well, even if their motion shouldn’t be described as normal diffusion. However, even if the effect yielded by the bumps on the membrane is more likely to be important at long times, it could start to show at short times already, manifesting itself in the diffusion coefficient as well.

The striking aspect emerging from Figure 4.5 is that even such a rough statistics shows a difference in the behaviour of high-curvature and low-curvature domains, the high-curvature domains being consistently characterised by a more modest displacement at all lag times. The difference in behaviour seems to become more evident with the increasing of the lag time,

apparently supporting the idea of a lag time-dependent effect previously suggested.

However, the analysis as described so far presents some serious flaws.

First of all, the radius of the domains is not taken into account at all, while it has been found [67, 10] that the diffusivity of L_d domains in a L_o continuous phase decreases with the increasing of the radius. Therefore the results in Figure 4.5 could be distorted by different radii distributions in the two sets of data (high- and low-curvature domains).

Moreover, the exact shape of the GUV when pressed against the PDMS surface is unknown, and attempts made to directly assess the contact area have been inconclusive because of lack of z-resolution. This is a problem because of the depth of field of the microscope, that yields focused images even of some domains which, due to the GUV curvature, are not in contact with the PDMS surface. The only control on this aspect is given by the eccentricity parameter in the tracking script: domains that are not in contact with the patterned surface because of the GUV curvature appear distorted as ellipses, since the objective records their projection on the focal plane.

Some solutions have thus been implemented to overcome the aforementioned problems.

4.2.2 Indirect assessment of the contact area

A possible non-contact of the membrane with the PDMS surface would result in an increase of the mean diffusivity of L_d domains with respect to the contact area (at least because if the membrane is not in contact with the bumps there is no curvature effect). In order to exploit this to assess how much of the focused area is in contact, the GUV is tracked and divided in 4 concentric regions (one circle and 3 annuli, see Figure 4.7). Domains are then divided depending on the region their centre falls in, and the mean diffusivity of domains for each region is plotted. The resulting plot is shown in Figure 4.8.

Looking at the trend of D versus the distance from the centre it is possible to approximatively determinate the radius of the region that is actually in contact with the PDMS surface (in the GUV Figure 4.8 refers to, it is 3/4 of the imaging area). This threshold value is then used to exclude from the MSD analysis all those domains that are further than it from the centre of the imaging area.

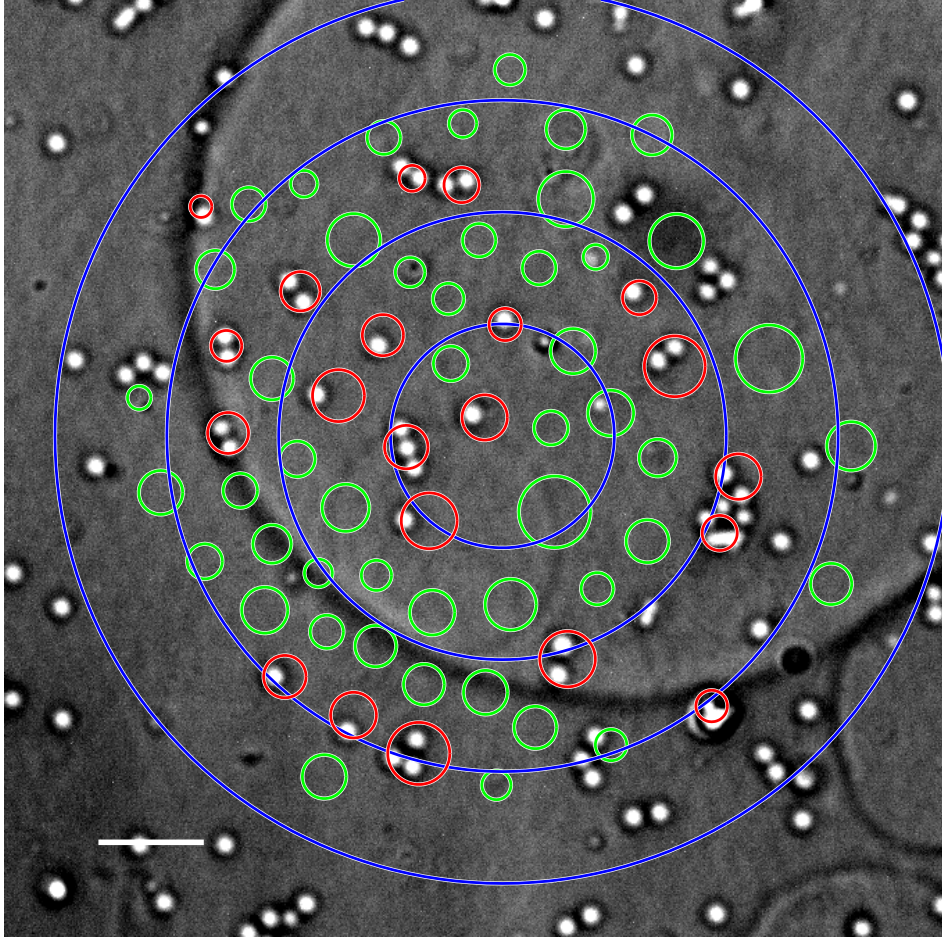


Figure 4.7 – Distance from the centre of the GUV. Frame extracted from the analysis explained in section 4.2.2. The largest blue rings outlines the GUV (as detected in the epifluorescence used to build this image), the others delimit the different regions the GUV is divided into. Domains are schematically represented as smaller circles, drawn using the positions and the radii as detected by the tracking software (in the epifluorescence image). Domains that were on a PDMS bump are in red, the others in green. The picture is then superposed to a bright field image of the PDMS surface. Scale bar is $10\mu m$.

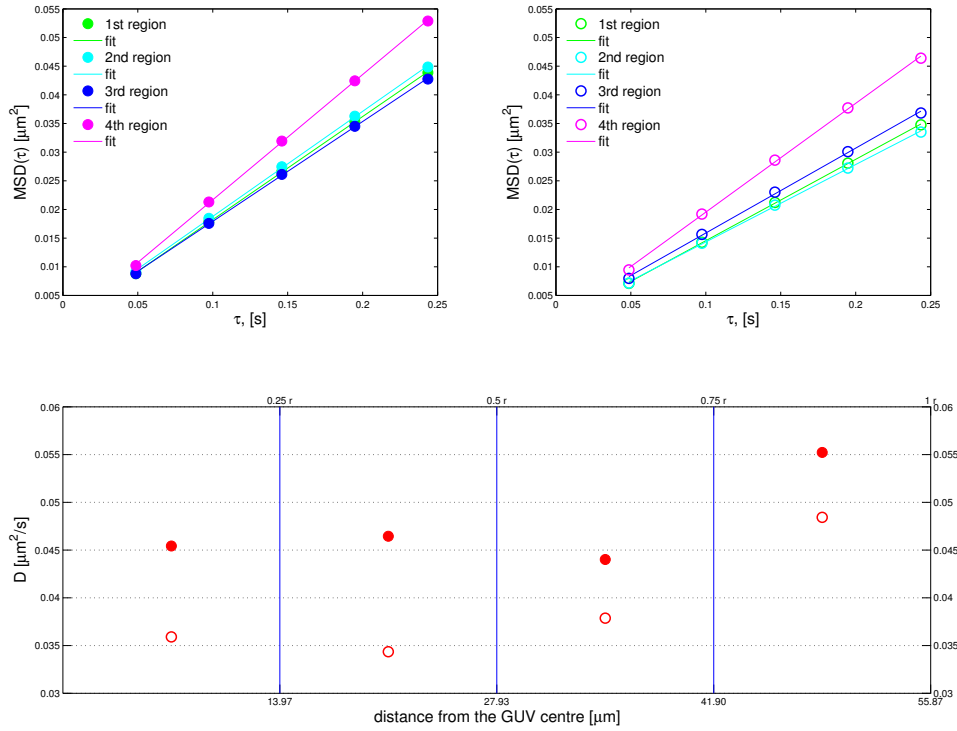


Figure 4.8 – There is an effect of the distance from the center of the GUV on domain motility. (top) First few points of the mean MSD curve calculated for domains in different regions of the GUV. Regions are numbered starting from the centre of the contact area, therefore the 1st is the inner circle and the 4th the outer annulus (see Figure 4.7). **(top, left)** shows the mean MSD curves for low-curvature domains, **(top, right)** for high-curvature ones. **(bottom)** The values of the coefficient diffusion as extracted from the fit of the curves in previous panels using equation (4.2.2). Full markers refers to low-curvature domains, empty markers to high-curvature domains. This plot shows a marked difference of diffusion coefficient between domains in the outer annulus and in the other three regions, possibly indicating that the GUV membrane is not in contact with the PDMS surface. Therefore, only the data for the three inner regions were analysed. Error bars are omitted as they are smaller than the markers.

It is worth to point out that, since this analysis is just a control step, the dependence of the diffusivity from the radius of the domain is still neglected (approximation that implies that the radii distribution of L_d domains is the same in the different annuli the GUV is divided into).

The amount of surface in contact, as determined with this method, varies from GUV to GUV, depending on their excess area (compared to a sphere, see section 2.3).

4.2.3 Dependence on the radius

The elimination of the dependence in the radius in the comparison of the MSD of L_d domains is achieved in two steps.

The MSD of the domains at a fixed lag time is plotted against the radius, for both domains on bumps and not on bumps. The trend of data points corresponding to low-curvature domains is then fitted using an empirical function, to extract an average behaviour. This is then considered to be the “expected” behaviour for L_d domains without externally imposed curvature in these experimental conditions.

The MSD of each high-curvature L_d domain is then plotted (at a fixed lag time) against the “expected” MSD corresponding to its radius. By doing so it is easy to highlight the difference in mobility between domains on and not on bumps, comparing the data points of domains on bumps with the 1:1 line: data points below it correspond to domains showing less mobility than the average obtained from the low-curvature domains, while points above the line correspond to more mobile domains. The plot obtained is shown in Figure 4.9.

The same procedure is applied to the diffusivity. The results for three different GUVs are shown in Figure 4.10.

It is worth to point out that in order to plot Figures 4.9 and 4.10 all the MSDs belonging to the same domain were averaged, yielding one data point for each domain (or two data points in case the domain was on a bump for just a fraction of the video). The uncertainties on the averaged data point are the standard deviations of the means.

From the data in Figure 4.10 it is apparent that the lipid membrane of the GUV shows an energetic preference for having high-curvature zones occupied by the low bending modulus phase: L_d domains, when on a PDMS feature, tend to stay there, showing less mobility than domains on flat areas.

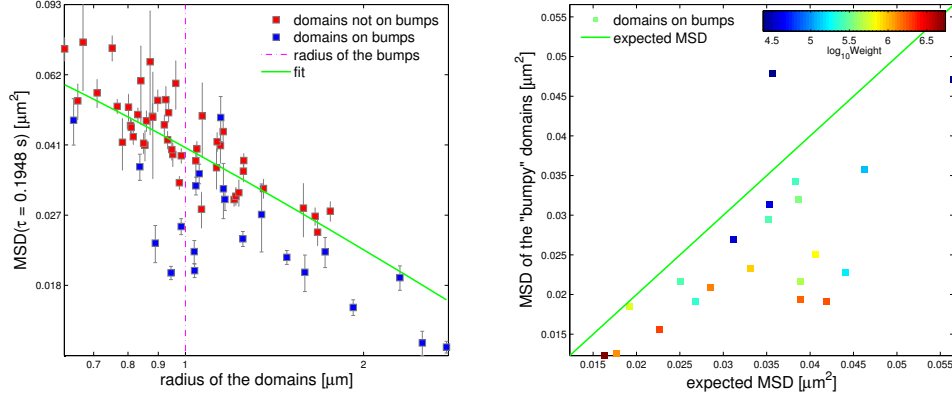


Figure 4.9 – Scatter plot of the Mean Square Displacement. Each data point represents the MSD of a different domain. **(left)** shows both low- and high-curvature domains (in red and blue respectively). The trend of domains not on bumps is then fitted with an empirical function ($MSD \propto 1/r$, showed in green), to obtain a “theoretical” behaviour of MSD as a function of the radius of the domains. In the plot on the **(right)** only the MSD of high-curvature domains are plotted, against the expected values obtained from the fit in the left plot (i.e. the value of MSD that each domain should have shown if it hadn’t been forced to assume a local, high curvature). The green line in the plot on the right is the 1:1 line. The colour of each data point shows its statistical weight ($1/\sigma^2$): the uncertainty of points in blue is one order of magnitude greater than that of red points. Both plots are in logarithmic scale on both axes. The magenta line in the plot on the **(left)** is just a reminder of the size of the PDMS features.

This seems to indicate the presence of an energy toll necessary to escape from the high-curvature feature.

This energetic barrier seems to be quite strong too, since in some cases it kept the L_d domains pinned on the PDMS bumps despite a moderate drift of the GUV, as it can be seen in Figure 4.11.

As shown in Figures 4.9 and 4.10, not all data points related to domains on a bump are below the empirical fit. Nevertheless, data points above it are characterised by an uncertainty one order of magnitude greater than data points below, therefore being far less significant.

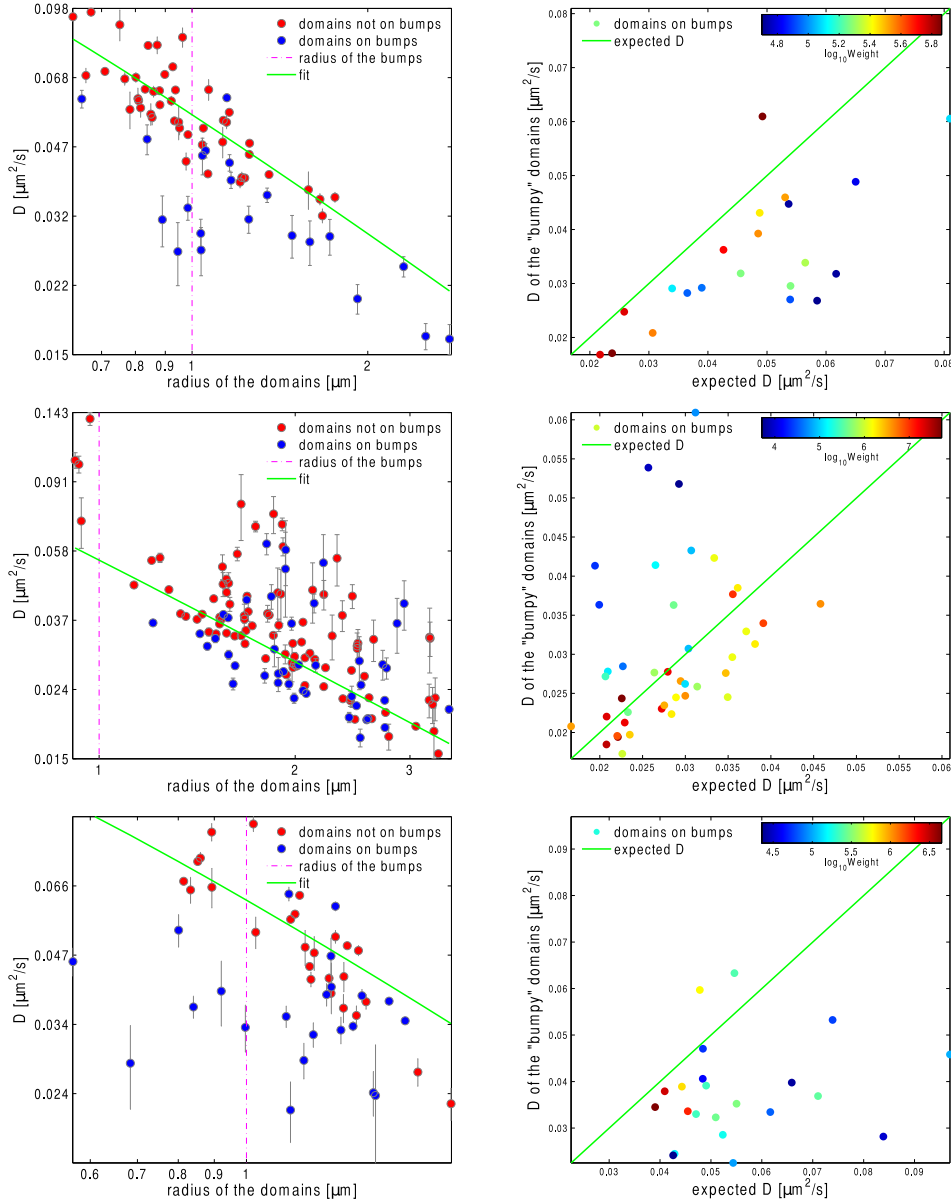


Figure 4.10 – Scatter plot of the diffusion coefficient, highlighting the reduced mobility of L_d domains on bumps. Each row shows, in logarithmic scale, the scatter plots of the diffusion coefficient, obtained following the same procedure as explained in section 4.2.3 for the scatter plot of the MSD shown in Figure 4.9. **(left)** Scatter plot of domains both on (blue) and not on (red) bumps. Red points are fitted with an empirical function to obtain an empirical dependence on the radius of the domains. Each high-curvature point is plotted in the graph on the **(right)** using as abscissa the expected value of the diffusion coefficient corresponding to its radius. Colour represents the statistical weight of each data point.

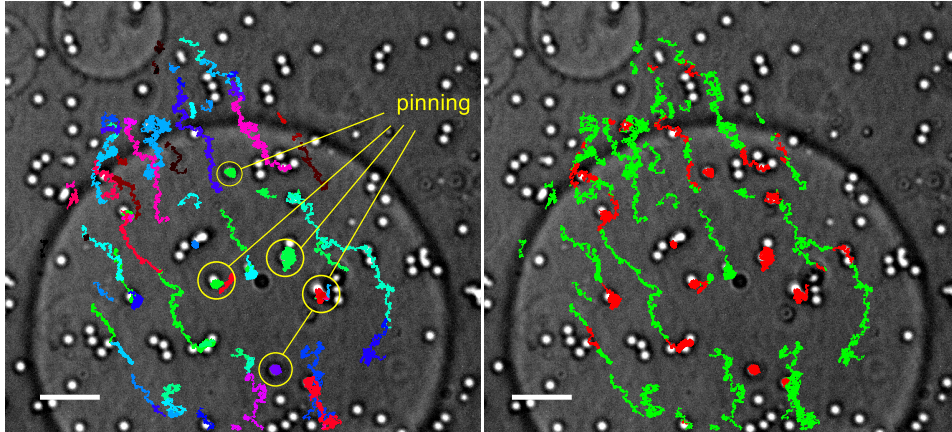


Figure 4.11 – Trapping despite the drift of the GUV. Here is shown a GUV that drifted (from top left to bottom right) during the imaging time, as shown by the trajectories of the domains (multicoloured lines in the **(left)** picture). Despite the drift, L_d domains got pinned on the PDMS features, as highlighted by the yellow circles. Some of them stayed still for the entire imaging time. **(right)** Same picture, highlighting in red the trajectories of L_d domains whenever they were on a PDMS bump.

4.3 Caging analysis

The analysis so far was concentrated on the first few points of the MSD curves, and confirmed that it is energetically favourable for the phase-separated membrane to laterally organise in order to place low bending modulus L_d domains at high-curvature features: L_d domains that with Brownian motion end up on a PDMS feature tend to stay on it, as shown in the previous sections.

However, to better highlight the trapping mechanism, the behaviour of L_d domains has to be observed at longer times.

The hypothesis that naturally surfaces when observing the data and the acquired videos is that the motion of a L_d domain placed on a PDMS bump should not be affected by it as long as the bump is far from the border of the L_d : as long as the only region deformed by the bump is the L_d region, the bending energy should be independent from the actual relative position of the bump and the domain. However, when the domain move so that the L_o phase starts to bend, the bending energy increases, thus making such movements not energetically favourable. The time at which the effects of such caging mechanism become visible is intrinsically dependent on the

radius of the L_d domain.

To analyse the behaviour of L_d domains at longer times, the $\text{MSD}(\tau)$ is calculated on 50 frames long segments ($\sim 2.5s$), instead of the 20 frames long ones used in section 4.2. The diffusion coefficients are then calculated by the fit of the first few (5) points of each MSD curve. By normalising each MSD curve with 4 times its diffusion coefficient, it is possible to compare curves of domains of different radius, even belonging to different vesicles. Of course, this normalisation causes a loss of information, but it highlights the aspect of interest in this section, namely the deviation of the behaviour of L_d domains placed on a PDMS bump from brownian motion. The normalised MSD curve of a domain moving of pure Brownian diffusion would be, following from equation (4.2.2), the identity line, while any domain whose motion is in any way confined would show a curve falling below that line.

To highlight the differences in the trend of the normalised curves depending on the radius of the domains, the L_d domains on bumps are divided in 3 groups of increasing radius, and compared to the curve of the domains not on bumps.

As shown in Figure 4.12 the difference in behaviour is evident between L_d domains on bumps and not on bumps, and it becomes more evident decreasing the radius. The $\text{MSD}/4D$ curve for small radius domains deviates early and significantly from the identity line, showing that movements on long time scales are hindered by a trapping mechanism. Increasing the radius, the deviation is less and less pronounced, trending toward the behaviour of L_d domains with no curvature constraints (i.e. not on a PDMS bump).

To better investigate this dependence on the radius, the same analysis was performed using smaller bins for the radius of the domains, i.e. averaging on less domains, but more similar in size (see Figure 4.13). A parameter was introduced to quantify the caging effects: the deviation of $\text{MSD}/4D$ curves from the identity line at a fixed lag time $\bar{\tau}$, defined as:

$$\left(\frac{\Delta h}{h}\right)\Big|_{\bar{\tau}} = \frac{\bar{\tau} - \text{MSD}(\bar{\tau})/4D}{\bar{\tau}}. \quad (4.3.1)$$

As the function that fits the trend of this deviation was not trivial to identify because of the small number of data points, a simple simulation was used to try and identify the right model describing this phenomenon.

Since I found it easier to simulate the problem in the coordinate system of the L_d domain, the simulation consisted in a single Brownian diffusor (the

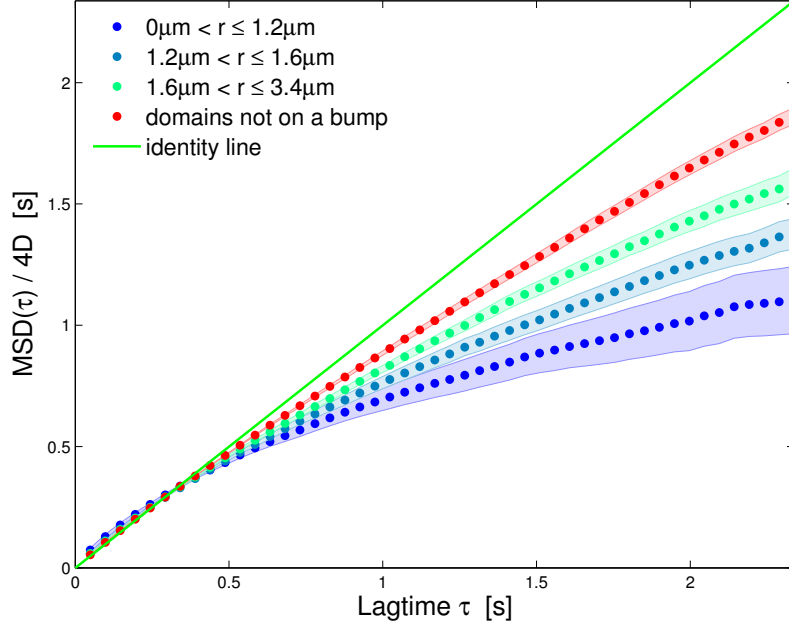


Figure 4.12 – Effects of caging: the MSD/4D curve deviates from the line describing the Brownian motion. Each MSD/4D curve is the average of several curves belonging to L_d domains with similar radii (see legend). The curve for domains moving of Brownian motion would overlap on the identity line (green), while any deviation below it is the signature of a confined motion.

bump), moving every step of a determined length in random directions but confined into a circular area. Of course, this simulation is rough and way too simple to describe the real experimental system.

The simulation was performed several times, varying the radius of the bounding circle. The MSD curve of the diffuser (calculated as described in section 4.2) was found to saturate as $aR^2 \left(1 - e^{-b\tau/R^2}\right)$, R being the radius of the bounding circle and a and b being constants. As the diffusion coefficient (proportional to the length of every step) was a constant in the simulation, the very same function described the behaviour of MSD/4D, the only difference being the value of a . From this it followed that, at fixed lag time $\bar{\tau}$,

$$\left(\frac{\Delta h}{h}\right)\Big|_{\bar{\tau}} = 1 - a'R^2 \left(1 - e^{-b\bar{\tau}/R^2}\right) \text{ with, in general, } a' \neq a. \quad (4.3.2)$$

In qualitative agreement with what found in the simulations, $(\Delta h/h)|_{\bar{\tau}} =$

$Ar^2(B - e^{-C\bar{\tau}/R^2})$, where r is the radius of the L_d domain and A , B , and C are constants, fits the experimental data for the deviation parameter shown in Figure 4.13.

On a side note, also the MSD/4D curve of L_d domains not on bumps is not a straight line, as it bends at long times. This is most likely because of membrane mediated, domain-domain interaction [70]. In vesicles with excess area, L_d domains can spontaneously have a different curvature than the surrounding L_o phase, therefore budding outwards or inwards the vesicle. When such two L_d domains are close the L_o phase is forced to bend, since the membrane is smooth and can not have any sharp edges. The bending of the L_o phase is associated to an energy toll, that is higher the closer the L_d domains are. This mechanism acts like a repulsive force between domains, hindering their coalescence, and it is visible on vesicles with excess area and the right proportion of L_d and L_o phases [70].

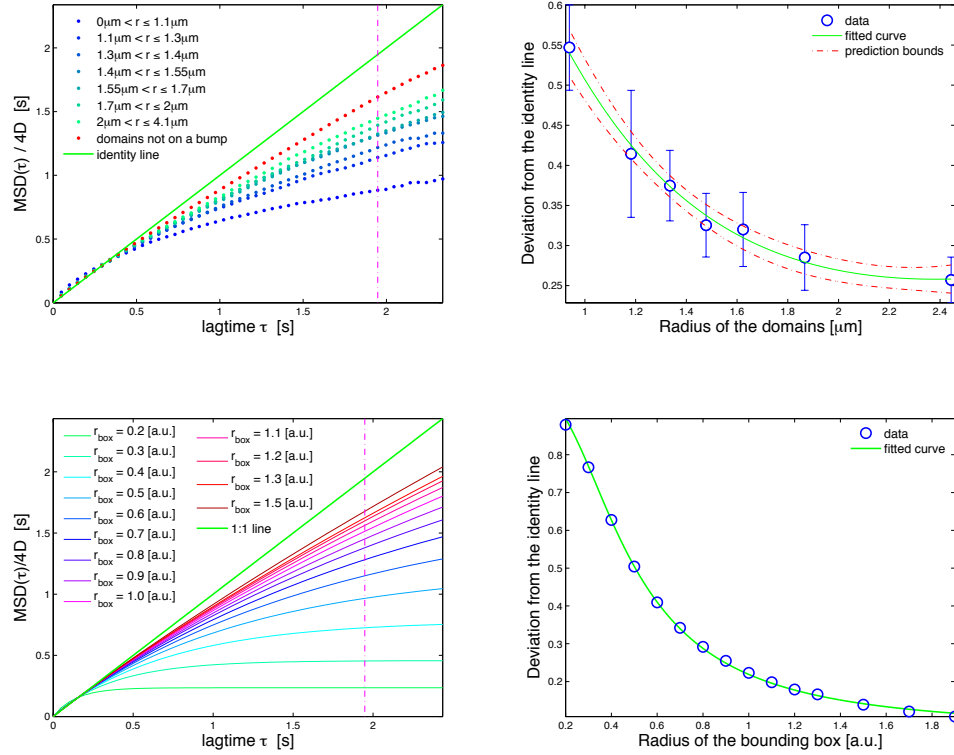


Figure 4.13 – Caging dependence on the radius, in qualitative agreement with confined Brownian motion simulations. The domains were grouped by their radius in narrower bins, in order to highlight the trend that surfaced in Figure 4.12. (a) are the curves thus obtained, while on the (b) is the trend of the parameter defined in equation (4.3.1). The error bars were not reported in the graph on the (a) to avoid overcrowding of the figure. The magenta line in the (a) graph marks the lag time at which the parameter to assess the deviation from the identity line is calculated. (c) MSD/4D curves for a simulated random walker whose motion is confined in a circular area. The green line is the identity line, and is the MSD/4D curve of pure Brownian diffusion. The magenta line marks the lag time at which the parameter to assess the deviation from the identity line is calculated. (d) shows the dependence of said parameter on the radius of the bounding box, fitted with equation (4.3.2)

4.4 Discussion

From the analysis reported in section 4.2 and 4.3 it is possible to draw some interesting remarks.

First of all, the lateral sorting of the lipid bilayer yielding L_d domains to be preferentially placed on high-curvature portions of the surface is observed in lipid vesicles. This finding is in agreement with experiments on Supported Lipid Bilayers (SLB) [59, 75, 58, 88]. At difference with SLBs, the present geometry allows the membrane to drift on the surface. The observation that pinning persists to membrane drifting seems to be compatible with the high difference in energy bending when the same curvature is applied to the two phases, as estimated in section 2.5. Another signal of the strength of the pinning is the fact that the only events of “depinning” observed were caused by a L_d domain substituting another one on a bump (see Figure 4.14).

The analysis of the dynamics of L_d domains is however the most promising aspect. The MSD analysis revealed, already at short timescales, an influence of the interaction between the membrane and the bumps on the motion of L_d domains. L_d domains on the bumps resulted to be less motile than domains not on a bump, being characterised by a lower value of the diffusion coefficient. However, this reduced motility seems to be nothing but a signal of a much more interesting aspect, that becomes evident when extending the MSD analysis to longer timescales. The results of the measures and the comparison with the simulations, as reported in section 4.3, point out that a L_d domain placed on a high-curvature feature qualitatively behaves as a Brownian diffuser in a confined region, whose extension is proportional to the radius of the domain. Further analysis in this direction may lead to a better understanding of the trapping mechanism.

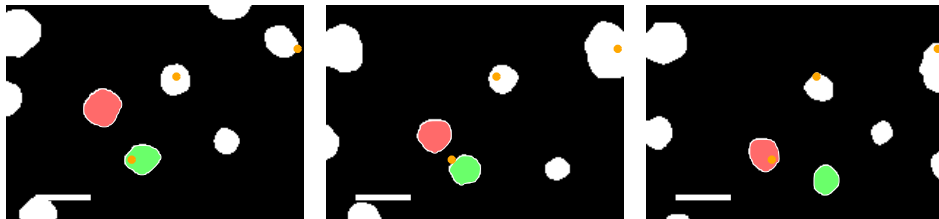


Figure 4.14 – Depinning due to domain-domain interaction. The L_d domain highlighted in red approaches the domain marked in green and takes its place on top on the PDMS bump (orange). Scale bar is $5\mu m$.

Chapter 5

Concluding remarks and future work

The work reported in this thesis can be divided in two parts.

In the first part, described in section 3.1, I developed a protocol for the preparation of a chemically homogeneous, microstructured surface. The strength of this protocol, based on soft lithography techniques, is that it can be modified in order to have different features structuring the surface. The size of the features achievable through this technique, with a few changes (as the employment of a clean room for the preparation), can reach the nanometric scale.

Such a versatile surface can have many applications as a substrate in lipid bilayer related experiments. For example, it can be used to investigate the effects of curvature in the growth of actin filaments [24].

In the second part of my work the microstructured surface was employed to force the lipid membrane of a Giant Unilamellar Vesicle to be locally bent, in order to investigate curvature-driven sorting mechanisms in liquid-liquid phase-separated ternary membranes of DPPC/diPhyPC/Cholesterol. Dynamic analysis on L_d domains shows that it is energetically favourable for the membrane to place L_d domains on the high-curvature regions, as the bending energy toll due to the forced curvature of the lipid membrane is lower because of the lower bending modulus of the L_d phase in comparison to the L_o phase. Mean Square Displacement analysis at long timescales of L_d domains placed on the high-curvature features has shown that their behaviour can be approximatively described by a Brownian diffusor confined

to a circular region.

These results offer inspiration for deeper investigations. For instance, in order to better understand the trapping mechanism that keeps L_d domains pinned on the high-curvature features, the rough simulations used in section 2.5 can be improved with a more realistic potential (including for example an harmonic term). This would enable us to extract physical parameters (e.g. the pinning potential) out of the experimental data.

The acquisition of new data may enable to conduct a statistical analysis comparing the percentage of high-curvature features occupied by L_d domains with their probability of being occupied in absence of any energetic gain (e.g. if the L_d domains were placed randomly).

More data together with a targeted analysis would also open the possibility to assess changes in the measured radius of L_d domains when migrating from a flat region to a high-curvature feature, and to study the relative position of the centre of L_d domains and the features. This would shed some light on the actual shape of the membrane in the close proximity of the micrometric features. N-body simulations could also be a valuable aid in doing so.

It would also be interesting to study “inverted” vesicles (i.e. with L_o domains in a continuous L_d phase), to verify that the L_o phase is reluctant to be placed on the bumps.

The final goal of these measurements would be of course a complete characterisation of the gain that the lateral organisation yields in terms of bending energy, that in turn would be an important step in the understanding of lateral organisation itself in phase-separated lipid membranes.

Bibliography

- [1] B. Alberts. *Molecular biology of the cell*. Routledge, 5th edition, 2000.
- [2] O. S. Andersen and R. E. Koeppe. Bilayer thickness and membrane protein function: an energetic perspective. *Annual review of biophysics and biomolecular structure*, 36:107–130, Jan. 2007.
- [3] A. G. Ayuyan and F. S. Cohen. Lipid peroxides promote large rafts: effects of excitation of probes in fluorescence microscopy and electrochemical reactions during vesicle formation. *Biophysical journal*, 91(6):2172–2183, Sept. 2006.
- [4] T. Baumgart, S. T. Hess, and W. W. Webb. Imaging coexisting fluid domains in biomembrane models coupling curvature and line tension. *Nature*, 425(6960):821–824, Oct. 2003.
- [5] R. Borsali and R. Pecora. *Soft-Matter Characterization*. Springer Verlag, 2008.
- [6] N. J. Brooks, O. Ces, R. H. Templer, and J. M. Seddon. Pressure effects on lipid membrane structure and dynamics. *Chemistry and physics of lipids*, 164(2):89–98, Feb. 2011.
- [7] A. R. Burns, D. J. Frankel, and T. Buranda. Local mobility in lipid domains of supported bilayers characterized by atomic force microscopy and fluorescence correlation spectroscopy. *Biophysical journal*, 89(2):1081–1093, Aug. 2005.
- [8] O. Cayre and V. Paunov. Contact angles of colloid silica and gold particles at air-water and oil-water interfaces determined with the gel trapping technique. *Langmuir*, 20(22):9594–9599, 2004.

- [9] S. M. Christensen and D. G. Stamou. Sensing-applications of surface-based single vesicle arrays. *Sensors*, 10(12):11352–1368, Jan. 2010.
- [10] P. Cicuta, S. L. Keller, and S. L. Veatch. Diffusion of liquid domains in lipid bilayer membranes. *The Journal of Physical Chemistry B*, 111(13):3328–3331, 2007.
- [11] M. D. Collins. Interleaflet coupling mechanisms in bilayers of lipids and cholesterol. *Biophysical journal*, 94(5):L32–L34, Mar. 2008.
- [12] M. D. Collins and S. L. Keller. Tuning lipid mixtures to induce or suppress domain formation across leaflets of unsupported asymmetric bilayers. *Proceedings of the National Academy of Sciences*, 105(1):124–128, Jan. 2008.
- [13] S. D. Connell, G. Heath, P. D. Olmsted, and A. Kisil. Critical point fluctuations in supported lipid membranes. *Faraday Discussions*, 161:91–111, 2013.
- [14] P. R. Cullis, M. J. Hope, and C. P. Tilcock. Lipid polymorphism and the roles of lipids in membranes. *Chemistry and physics of lipids*, 40(2):127–144, 1986.
- [15] J. H. Davis, J. J. Clair, and J. Juhasz. Phase equilibria in DOPC/DPPC-d62/cholesterol mixtures. *Biophysical journal*, 96(2):521–539, Jan. 2009.
- [16] R. F. M. de Almeida, A. Fedorov, and M. Prieto. Sphingomyelin/phosphatidylcholine/cholesterol phase diagram: boundaries and composition of lipid rafts. *Biophysical journal*, 85(4):2406–2416, Oct. 2003.
- [17] C. Dietrich, L. A. Bagatolli, Z. N. Volovyk, N. L. Thompson, M. Levi, K. Jacobson, and E. Gratton. Lipid rafts reconstituted in model membranes. *Biophysical journal*, 80(3):1417–1428, Mar. 2001.
- [18] M. Edidin. Shrinking patches and slippery rafts: scales of domains in the plasma membrane. *Trends in cell biology*, 11(12):492–496, Dec. 2001.
- [19] D. M. Engelman. Membranes are more mosaic than fluid. *Nature*, 438(7068):578–580, Dec. 2005.

- [20] R. Epanand. Membrane Lipid Polymorphism. In *Methods in Membrane Lipids*, volume 400, pages 15–26. Springer, 2007.
- [21] W. H. Evans and W. G. Hardison. Phospholipid, cholesterol, polypeptide and glycoprotein composition of hepatic endosome subfractions. *The Biochemical journal*, 232:33–36, Nov. 1985.
- [22] N. Fa, L. Lins, P. J. Courtoy, Y. Dufrêne, P. Van Der Smissen, R. Bras-seur, D. Tyteca, and M.-P. Mingeot-Leclercq. Decrease of elastic moduli of DOPC bilayers induced by a macrolide antibiotic, azithromycin. *Biochimica et Biophysica Acta (BBA)-Biomembranes*, 1768(7):1830–1838, July 2007.
- [23] W. R. Fletcher. *Equilibrium and non-equilibrium behaviour in phase separated lipid vesicles with fine temperature control*. PhD thesis, 2013.
- [24] J. Gallop and A. Walrant. Phosphoinositides and membrane curvature switch the mode of actin polymerization via selective recruitment of toca-1 and Snx9. *Proceedings of the National Academy of Sciences*, 110(18):7193–7198, Apr. 2013.
- [25] L. Gitlin, P. Schulze, and D. Belder. Rapid replication of master structures by double casting with PDMS. *Lab on a chip*, 9(20):3000–3002, Oct. 2009.
- [26] F. M. Goñi, A. Alonso, L. A. Bagatolli, R. E. Brown, D. Marsh, M. Prieto, and J. L. Thewalt. Phase diagrams of lipid mixtures relevant to the study of membrane rafts. *Biochimica et Biophysica Acta (BBA)-Molecular and Cell Biology of Lipids*, 1781(11):665–684, 2008.
- [27] Y. Graziani and A. Livne. Water Permeability of Bilayer Lipid Membranes: Sterol-Lipid Interaction. *The Journal of Membrane Biology*, 7(1):275–284, 1972.
- [28] L. S. Hirst, P. Uppamoochikkal, and C. Lor. Phase separation and critical phenomena in biomimetic ternary lipid mixtures. *Liquid Crystals*, 38(11-12):1735–1747, Nov. 2011.
- [29] C. Hofsäss, E. Lindahl, and O. Edholm. Molecular dynamics simulations of phospholipid bilayers with cholesterol. *Biophysical journal*, 84(4):2192–2206, Apr. 2003.

- [30] A. R. Honerkamp-Smith, P. Cicuta, M. D. Collins, S. L. Veatch, M. den Nijs, M. Schick, and S. L. Keller. Line tensions, correlation lengths, and critical exponents in lipid membranes near critical points. *Biophysical journal*, 95(1):236–246, July 2008.
- [31] A. R. Honerkamp-Smith, S. L. Veatch, and S. L. Keller. An introduction to critical points for biophysicists; observations of compositional heterogeneity in lipid membranes. *Biochimica et Biophysica Acta (BBA)-Biomembranes*, 1788(1):53–63, Jan. 2009.
- [32] M. Hope, M. Bally, G. Webb, and P. Cullis. Production of large unilamellar vesicles by a rapid extrusion procedure. Characterization of size distribution, trapped volume and ability to maintain a membrane potential. *Biochimica et Biophysica Acta (BBA)-Biomembranes*, 812(1):55–65, 1985.
- [33] T. Idema, S. Semrau, C. Storm, and T. Schmidt. Membrane Mediated Sorting. *Physical Review Letters*, 104(19):198102, May 2010.
- [34] L. Isa, F. Lucas, R. Wepf, and E. Reimhult. Measuring single-nanoparticle wetting properties by freeze-fracture shadow-casting cryo-scanning electron microscopy. *Nature communications*, 2:438, Jan. 2011.
- [35] J. Israelachvili. *Intermolecular and Surface forces, Third edition*. Academic Press, 3rd edition, 2011.
- [36] F. Jülicher and R. Lipowsky. Shape transformations of vesicles with intramembrane domains. *Physical Review E*, 53(3):2670–2683, 1996.
- [37] G. Khelashvili and B. Kollmitzer. Calculating the Bending Modulus for Multicomponent Lipid Membranes in Different Thermodynamic Phases. *Journal of chemical theory and computation*, 9(9):3866–3871, 2013.
- [38] W. Knoll, K. Ibel, and E. Sackmann. Small-angle neutron scattering study of lipid phase diagrams by the contrast variation method. *Biochemistry*, 20(22):6379–6383, 1981.
- [39] J. Korlach and P. Schwille. Characterization of lipid bilayer phases by confocal microscopy and fluorescence correlation spectroscopy. *Proceedings of the National Academy of Sciences*, 96(15):8461–8466, 1999.

- [40] R. D. Kornberg and H. M. McConnell. Inside-outside transitions of phospholipids in vesicle membranes. *Biochemistry*, 10(7):1111–1120, Mar. 1971.
- [41] A. Kusumi and Y. Sako. Cell surface organization by the membrane skeleton. *Current opinion in cell biology*, 8(4):566–574, 1996.
- [42] Y. G. Kuznetsov and A. McPherson. Atomic force microscopy in imaging of viruses and virus-infected cells. *Microbiology and molecular biology reviews*, 75(2):268–285, June 2011.
- [43] Y. Lange, J. Dolde, and T. Steck. The Rate of Transmembrane Movement of Cholesterol in the Human Erythrocyte. *Journal of Biological Chemistry*, 256(11):5321–5323, 1981.
- [44] J. C. Lawrence, D. E. Saslowsky, J. Michael Edwardson, and R. M. Henderson. Real-Time Analysis of the Effects of Cholesterol on Lipid Raft Behavior Using Atomic Force Microscopy. *Biophysical Journal*, 84(3):1827–1832, Mar. 2003.
- [45] M. Lessel, O. Bäümchen, and M. Klos. Self-assembled silane monolayers: A step-by-step high speed recipe for high-quality, low energy surfaces. *arXiv preprint arXiv*, 1212(0998):29–31, 2012.
- [46] B. A. Lewis and D. M. Engelman. Lipid bilayer thickness varies linearly with acyl chain length in fluid phosphatidylcholine vesicles. *Journal of molecular biology*, 166(2):211–217, May 1983.
- [47] H. Lindsey, N. O. Petersen, and S. I. Chan. Physicochemical characterization of 1,2-diphytanoyl-sn-glycero-3-phosphocholine in model membrane systems. *Biochimica et Biophysica Acta (BBA)-Biomembranes*, 555(1):147–167, July 1979.
- [48] R. Lipowsky and R. Dimova. Domains in membranes and vesicles. *Journal of Physics: Condensed Matter*, 15(1):S31–S45, Jan. 2003.
- [49] E. London and D. A. Brown. Insolubility of lipids in triton X-100: physical origin and relationship to sphingolipid/cholesterol membrane domains (rafts). *Biochimica et Biophysica Acta (BBA)-Biomembranes*, 1508(1):182–195, Nov. 2000.

- [50] J. A. Lundbaek, O. S. Andersen, T. Werge, and C. Nielsen. Cholesterol-induced protein sorting: an analysis of energetic feasibility. *Biophysical journal*, 84(3):2080–2089, Mar. 2003.
- [51] J. A. Lundbaek, S. A. Collingwood, H. I. Ingólfsson, R. Kapoor, and O. S. Andersen. Lipid bilayer regulation of membrane protein function: gramicidin channels as molecular force probes. *Journal of the Royal Society Interface*, 7(44):373–395, Mar. 2010.
- [52] S. J. Marrink, H. J. Risselada, S. Yefimov, D. P. Tieleman, and A. H. de Vries. The MARTINI force field: coarse grained model for biomolecular simulations. *The Journal of Physical Chemistry B*, 111(27):7812–7824, July 2007.
- [53] L. Mayer, M. Hope, and P. Cullis. Vesicles of variable sizes produced by a rapid extrusion procedure. *Biochimica et Biophysica Acta (BBA)-Biomembranes*, 858(1):161–168, 1986.
- [54] G. Meer. Lipid traffic in animal cells. *Annual review of cell biology*, 5(1):247–275, 1989.
- [55] O. G. Mouritsen. Lipids, curvature, and nano-medicine. *European journal of lipid science and technology*, 113(10):1174–1187, Oct. 2011.
- [56] F. A. Nezil and M. Bloom. Combined influence of cholesterol and synthetic amphiphilic peptides upon bilayer thickness in model membranes. *Biophysical journal*, 61(5):1176–1183, May 1992.
- [57] C. Nicolini, A. Celli, E. Gratton, and R. Winter. Pressure tuning of the morphology of heterogeneous lipid vesicles: a two-photon-excitation fluorescence microscopy study. *Biophysical journal*, 91(8):2936–2942, Oct. 2006.
- [58] M. O. Ogunyankin and M. L. Longo. Compositional sorting dynamics in coexisting lipid bilayer phases with variations in underlying e-beam formed curvature pattern. *Analyst*, 138:3719–3727, July 2013.
- [59] R. Parthasarathy, C.-h. Yu, and J. T. Groves. Curvature-modulated phase separation in lipid bilayer membranes. *Langmuir*, 22(11):5095–5099, 2006.

- [60] V. Paunov. Novel Method for Determining the Three-Phase Contact Angle of Colloid Particles Adsorbed at Air-Water and Oil-Water Interfaces. *Langmuir*, 19(19):7970–7976, 2003.
- [61] V. Paunov and O. Cayre. The Gel Trapping Technique: A Novel Method for Characterizing the Wettability of Microparticles and the Replication of Particle Monolayers. *Materials Research Society Symposium Proceedings*, EXS(2):25–27, 2004.
- [62] E. P. Petrov and P. Schwille. Translational diffusion in lipid membranes beyond the Saffman-Delbruck approximation. *Biophysical journal*, 94(5):L41–L43, Mar. 2008.
- [63] P. Pieranski. Two-Dimensional Interfacial Colloidal Crystals. *Physical Review Letters*, 45(7):569–572, 1980.
- [64] A. Pralle, P. Keller, E. L. Florin, K. Simons, and J. K. Hörber. Sphingolipid-cholesterol rafts diffuse as small entities in the plasma membrane of mammalian cells. *The Journal of cell biology*, 148(5):997–1008, Mar. 2000.
- [65] J. Rogers and R. Nuzzo. Recent progress in soft lithography. *Materials today*, 8(2):50–56, 2005.
- [66] R. Rusinova, E. A. Hobart, R. E. Koeppe, and O. S. Andersen. Phosphoinositides alter lipid bilayer properties. *The Journal of general physiology*, 141(6):673–690, June 2013.
- [67] P. Saffman and M. Delbrück. Brownian motion in biological membranes. *Proceedings of the National Academy of Sciences*, 72(8):3111–3113, 1975.
- [68] S. A. Safran. *Statistical thermodynamics of surfaces, interfaces, and membranes*. Addison-Wesley Reading, MA, 1994.
- [69] A. V. Samsonov, I. Mihalyov, and F. S. Cohen. Characterization of cholesterol-sphingomyelin domains and their dynamics in bilayer membranes. *Biophysical journal*, 81(3):1486–1500, Sept. 2001.
- [70] S. Semrau, T. Idema, T. Schmidt, and C. Storm. Membrane-mediated interactions measured using membrane domains. *Biophysical journal*, 96(12):4906–4915, June 2009.

- [71] J. R. Silvius. Thermotropic phase transitions of pure lipids in model membranes and their modifications by membrane proteins. In *Lipid-protein interactions 2*, pages 239–281. 1982.
- [72] K. Simons and E. Ikonen. Functional rafts in cell membranes. *Nature*, 387(6633):569–572, June 1997.
- [73] J. Song and R. E. Waugh. Bending rigidity of SOPC membranes containing cholesterol. *Biophysical journal*, 64(6):1967–1970, June 1993.
- [74] E. H. Stanley. *Introduction to Phase Transitions and Critical Phenomena*. Oxford University Press, 1987.
- [75] A. Subramaniam. Particle/fluid interface replication as a means of producing topographically patterned polydimethylsiloxane surfaces for deposition of lipid bilayers. *Advanced Materials*, 22(19):2142–2147, May 2010.
- [76] L. Ting and S. Feghhi. Effect of Silanization Film Thickness in Soft Lithography of Nanoscale Features. *Journal of Nanotechnology in Engineering and Medicine*, 2(4):041006, 2011.
- [77] M. J. Uline and I. Szleifer. Mode specific elastic constants for the gel, liquid-ordered, and liquid-disordered phases of DPPC/DOPC/cholesterol model lipid bilayers. *Faraday Discussions*, 161:177–191, 2013.
- [78] P. Uppamoochikkal, S. Tristram-Nagle, and J. F. Nagle. Orientation of tie-lines in the phase diagram of DOPC/DPPC/cholesterol model biomembranes. *Langmuir*, 26(22):17363–17368, Nov. 2010.
- [79] S. L. Veatch, P. Cicuta, P. Sengupta, A. Honerkamp-Smith, D. Holowka, and B. Baird. Critical fluctuations in plasma membrane vesicles. *ACS chemical biology*, 3(5):287–293, May 2008.
- [80] S. L. Veatch, K. Gawrisch, and S. L. Keller. Closed-loop miscibility gap and quantitative tie-lines in ternary membranes containing diphytanoyl PC. *Biophysical journal*, 90(12):4428–4436, June 2006.
- [81] S. L. Veatch and S. L. Keller. Organization in Lipid Membranes Containing Cholesterol. *Physical Review Letters*, 89(26):268101, Dec. 2002.

- [82] S. L. Veatch and S. L. Keller. Separation of liquid phases in giant vesicles of ternary mixtures of phospholipids and cholesterol. *Biophysical journal*, 85(5):3074–3083, Nov. 2003.
- [83] S. L. Veatch and S. L. Keller. Seeing spots: complex phase behavior in simple membranes. *Biochimica et Biophysica Acta (BBA)-Molecular Cell Research*, 1746(3):172–185, Dec. 2005.
- [84] S. L. Veatch, O. Soubias, S. L. Keller, and K. Gawrisch. Critical fluctuations in domain-forming lipid mixtures. *Proceedings of the National Academy of Sciences*, 104(45):17650–5, Nov. 2007.
- [85] D. Voet and J. G. Voet. *Biochemistry*. John Wiley & Sons, 4th edition, 2010.
- [86] R. Winter and C. Jeworrek. Effect of pressure on membranes. *Soft Matter*, 5(17):3157–3173, 2009.
- [87] Y. Xia and G. Whitesides. Soft lithography. *Annual review of materials science*, 28(1):153–184, 1998.
- [88] T.-Y. Yoon, C. Jeong, S.-W. Lee, J. H. Kim, M. C. Choi, S.-J. Kim, M. W. Kim, and S.-D. Lee. Topographic control of lipid-raft reconstitution in model membranes. *Nature materials*, 5(4):281–285, Apr. 2006.
- [89] Y. Z. Yoon, J. P. Hale, P. G. Petrov, and P. Cicuta. Mechanical properties of ternary lipid membranes near a liquid-liquid phase separation boundary. *Journal of physics. Condensed matter*, 22(6):062101, Feb. 2010.

Acknowledgements

I would like to thank my supervisors, Luigi Cristofolini and Pietro Cicuta, for sharing their extensive experience and for closely following me during this work.

I would also like to thank Will Fletcher, Jurij Kotar and Eileen Nugent for their help and advice, respectively in the GUV preparation, in the image acquisition and in the processing of PDMS.

I will be eternally grateful to Nicolas Bruot, Eugenia Cammarota, Lorenzo Di Michele, Avelino Javer, Stefano Pagliara, and Lucia Parolini for their friendship and advice (and the cakes and pastries eaten near the vending machines, and the pizza, and the bicycle, and I could go on and on but I will stop here).

A thank you is a must to the ERASMUS program, that gave me the opportunity of conducting such a meaningful experience in Cambridge.

Last, but not least, I would like to thank my family (my mother and my sister in particular) for supporting me and for being close to me in my every choice in the path that lead to this moment.